Hierarchically Structured Vanadium Pentoxide–Polymer Hybrid Materials

Ulrich Tritschler,[†,#] Igor Zlotnikov,[‡,#] Paul Zaslansky,[§] Peter Fratzl,[‡] Helmut Schlaad,[⊥,*] and Helmut Cölfen[†,*]

[†]Physical Chemistry, University of Konstanz, Universitätsstraße 10, D-78457 Konstanz, Germany, [‡]Department of Biomaterials, Max Planck Institute of Colloids and Interfaces, Research Campus Golm, D-14424 Potsdam, Germany, [§]Berlin Brandenburg Center for Regenerative Therapies/Julius Wolff Institute, Charité—Universitätsmedizin Berlin, D-13353 Berlin, Germany, and [⊥]Department of Colloid Chemistry, Max Planck Institute of Colloids and Interfaces, Research Campus Golm, D-14424 Potsdam, Germany. [#]U. Tritschler and I. Zlotnikov contributed equally.

ABSTRACT Biomimetic composite materials consisting of vanadium pentoxide (V_2O_5) and a liquid crystal (LC) "gluing" polymer were manufactured exhibiting six structural levels of hierarchy, formed through LC phases. The organic matrix was a polyoxazoline with pendant cholesteryl and carboxyl units, forming a lyotropic phase with the same structural orientation extending up to hundreds of micrometers upon shearing, and binding to V_2O_5 *via* hydrogen bridges. Composites consisting of V_2O_5–LC polymer hybrid fibers with a pronounced layered structuring were obtained. The V_2O_5–LC polymer hybrid fibers consist of aligned V_2O_5 ribbons, composed of self-assembled V_2O_5 sheets, encasing a chiral nematic polymer matrix. The structures of the V_2O_5–LC polymer composites strongly depend on the preparation method, *i.e.*, the phase-transfer method from aqueous to organic medium, in which the polymer forms LC phases. Notably, highly defined micro- and nanostructures were obtained when initiating the synthesis using V_2O_5 tactoids with preoriented nanoparticle building units, even when using isotropic V_2O_5 dispersions. Shear-induced hierarchical structuring of the composites was observed, as characterized from the millimeter and micrometer down to the nanometer length scales using complementary optical and electron microscopy, SAXS, μCT, and mechanical nanoindentation.

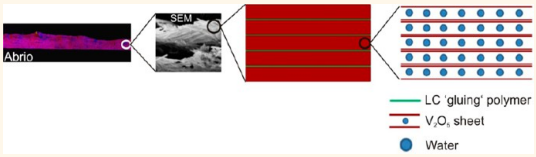

KEYWORDS: vanadium pentoxide · liquid crystal · hierarchical structure · organic–inorganic composite material · biomimetic

Natural organic–inorganic biomaterials, in which stiff and brittle mineral crystals are joined by soft and ductile biopolymers,[1,2] exhibit a sophisticated hierarchical structuring and a well controlled coupling at the interface between organic and inorganic components. These structural motives influence the material mechanical properties, contributing to both strength and toughness.[3−6] A prominent and well-studied biomineral examp is nacre, which consists of 95% aragonitic $CaCO_3$ polymorph, but exhibits 3000 times higher fracture resistance than pure aragonite.[3] The inorganic platelets are the load-bearing component that is responsible for the relatively high stiffness of the composite. The unique combination betweeen stiffness and toughness of the nacre results from the internal structure of the aragonite,[7,8] staggered arrangement of the platelets within the polymeric matrix,[5,9] and interface properties,[10−14] including interface features such as nanoasperities and mineral bridges.[13,15] This type of arrangement also provides flexibility to the entire structure by increasing the deformability of the organic matrix.[16]

Inspired by the structure and remarkable properties of these materials, biomimetic lamellar composite structures were developed, predominantely by using micro- and nanoplatelets, and in particular clay minerals, montmorillonite, and Laponite clay platelets, as well as alumina platelets. Manifold nacre mimicking approaches were reported including, for example, the self-assembly of Na/Ca montmorillonite platelets,[17] and the layer-by-layer assembly of clay-polyelectrolyte multilayers.[18−22] Mulitlayered polymer-clay nanocomposites were also fabricated by doctor blading,[23] and solution casting procedures were used to synthesize disco-nematic liquid crystalline structures of Laponite nanoplatelets within an amorphous poly (ethylene glycol) (PEG) matrix.[24] Microelectromechanical systems technology was used to produce microcomposite materials mimicking the cross-lamellar microarchitecture of molluscan shells and showing features such as energy-dissipating cracking patterns.[25] Composite materials were obtained by Bonderer *et al.*[26] *via* a bottom-up colloidal assembly of alumina

* Address correspondence to helmut.schlaad@mpikg.mpg.de, helmut.coelfen@uni-konstanz.de.

Received for review February 26, 2014 and accepted April 9, 2014.

Published online April 09, 2014
10.1021/nn501153u

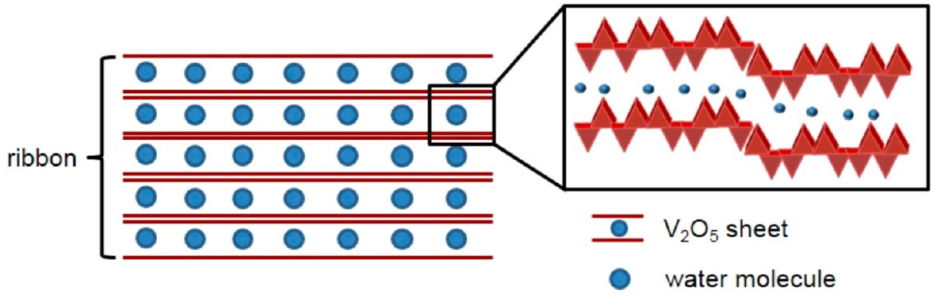

Scheme 1. Description of vanadium pentoxide (V_2O_5) structure.

platelets within a chitosan matrix that exhibit both high tensile strength and ductile behavior. Ceramic-based materials were fabricated by ice-templating methods.[27,28] Most notable in this context are the materials synthesized by Munch *et al.*[29] that exhibit the highest fracture toughness reported to date, even outperforming natural nacre. Erb *et al.*[29] reported the fabrication of hierarchically reinforced, wear-resistant materials containing micrometer-sized reinforcing anisotropic particles coated with superparamagnetic magnetite nanoparticles, thus allowing control over orientation and distribution of the magnetically responsive reinforcing particles in the composites by means of only weak magnetic fields. Very recently, we addressed the hierarchical structuring of biomaterials from the nanometer length scale up to hundreds of micrometers by synthesizing liquid crystal (LC) polymer−Laponite composite materials structured on three hierarchical levels by one-step self-organization. The organic component was a polyoxazoline with pendant cholesteryl and carboxyl (*N*-Boc-protected amino acid) side chains, enabling the polymer to form a chiral nematic lyotropic phase, thus forming two hierarchical levels, and to bind to the positively charged rims of Laponite nanoplatelets. Long-range orientation of the polymeric LC phase was induced by shearing. The Laponite clay nanoparticles that are also able to form a liquid crystalline phase due to their anisotropic shape[30,31] assemble into a mesocrystalline arrangement within the LC polymer matrix and consequently form the third level of the hierarchical structuring.[32]

Another interesting material known to have charged anisotropic particles is vanadium pentoxide (V_2O_5). It is thus a good candidate for the above described liquid crystal driven hierarchical structuring. V_2O_5−H_2O was already found in the 1920s by Zocher *et al.*[33−36] to form tactoid sol phases and is chemically classified as a lyotropic, inorganic, nematic liquid crystal.[37,38] The tactoids are composed of rod-shaped nanoparticles, which are mutually oriented in a nematic and anisotropic manner.[39,40] To clarify the notions used in the following text, we present a model of the V_2O_5 structure, adapted from literature.[39,41−44] V_2O_5 is composed of V_2O_5 sheets (consisting each of two V_2O_5 layers, made of square pyramidal VO_5 units), which are separated by intercalated water molecules with a defined intersheet distance. Stacking of these V_2O_5 sheets forms ribbons (rod-like primary ribbons), which then can arrange into fibers and layers (see Scheme 1).

Only very recently, Burghard *et al.*[42] reported the fabrication of paper-like materials mimicking structural biomaterials by making use of the ability of V_2O_5 sheets to self-assemble. Lausser *et al.*[45] recently succeeded in forming V_2O_5 mesocrystals,[46,47] which are superstructures possessing 3D mutual order of the nanocrystal building units. By starting from a V_2O_5 tactoid consisting of preoriented nanoparticle building units V_2O_5 mesocrystals were obtained *via* three different ways: addition of salt, application of a strong external sedimentation force, and addition of a surface-active polymer. The approach of adding a surface-active polymer that adsorbs and stabilizes the oxygen terminated (020) faces of V_2O_5 was found to be superior to the other two approaches. This is due to the defining shape and alignment of primary V_2O_5 ribbons, reducing the repulsive forces of the superstructure building units. The concept of mesocrystal formation and nonclassical crystallization is well established in the field of biomineralization[7,48−55] as well as for the development of biomimetic composite structures in the context of improved material properties.[46,56−59] In this regard, vanadium oxides, and vanadium pentoxide in particular, are of high interest due to their broad range of applications, *e.g.*, in the field of electrochromic/-optical devices,[60−63] electrochemistry,[64−66] electrodes for lithium batteries,[67−70] catalysis,[71−76] gas sensors,[77−80] and photocatalytic reactions.[81−83] The importance of V_2O_5 nanoparticles acting as catalysts was only recently shown by their peroxidase-like activity[84] as well as their intrinsic bromination activity, mimicking vanadium haloperoxidases that prevent marine biofouling.[85] Due to the layered structuring of V_2O_5, it is used as an intercalation material.[86−96] Defined nano- and mesostructures of vanadium oxide materials considerably enhance the material's capacities for sensing[97] as well as for energy-storage devices[98] in comparison to bulk vanadium oxide. For example, the mechanical deformation effect by intercalation of ions

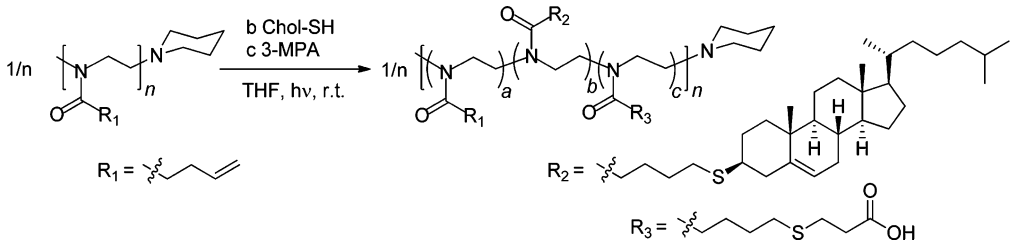

Scheme 2. Simultaneous modification of poly[2-(3-butenyl)-2-oxazoline] with thiocholesterol (Chol-SH) and 3-mercaptopropionic acid (3-MPA) by thiol−ene photochemistry.

in vanadium oxide was used to mimic human skeletal muscle.[99]

Hierarchical structuring of polymers was demonstrated by the self-assembly of peptide-based block copolymers[100] or rod-coil block copolymers,[101] and by self-assembly of hierarchical block copolymers for structuring nanoparticles.[102] LC-driven self-assembly of polymers, a concept also found in many biological systems,[103] enabled mimicking of the optical and structural properties of the golden beetle *Chrysina resplendens*.[104] Self-assembly of lyotropic liquid crystals granted access to materials possessing defined porous structuring,[105−109] and in addition to mesoporosity, chiral long-range orientation was induced into materials by using chiral surfactants[110,111] or nanocrystalline cellulose.[112]

Here we apply our fabrication concept for hierarchically structured composite materials[32] to the synthesis of biomimetic LC "gluing" polymer−V_2O_5 composites *via* a one-step self-organization on six hierarchical levels. The V_2O_5 sheets self-assemble into V_2O_5 ribbons (first level), to which the copolymer binds *via* the carboxylate gluing units to form a V_2O_5−polymer hybrid material. The copolymer cholesteryl side chains form a chiral nematic LC phase (second and third hierarchical level). The V_2O_5 ribbons assemble with LC polymer in between, herein called fibers, laying flat parallel to the surface (fourth level), finally building up a composite material with a layered structuring in the horizontal dimension (fifth level) and a textured substructure in the vertical dimension (sixth level).

RESULTS AND DISCUSSION

Polymer Synthesis. The copolymer used for synthesizing organic−inorganic composite materials contained cholesteryl side chains, which are able to form lyotropic phases, and carboxylates, enabling the polymer to selectively bind to positively charged nanoparticle faces[32] or, at acidic pH, form hydrogen bridges with surface oxygens.[45] For this, poly[2-(3-butenyl)-2-oxazoline] (PBOx) (number-average molecular weight, M_n = 7.2 kg mol^{-1}, MALDI-ToF MS (see Figure S1 in the SI), dispersity M_w/M_n = 1.1, GPC) was functionalized by the simultaneous coaddition of thiocholesterol (Chol-SH) and 3-mercaptopropionic acid (3-MPA) (see Scheme 2).[32] Depending on the amount of Chol-SH and 3-MPA used, the composition of the purified product PBOx-Chol-MPA was found to be [C═C]/[Chol]/[COOH] = a/b/c = 0.53−0.49:0.18−0.22:0.31−0.35, by ^{1}H NMR spectroscopy (see Figure S2 in the SI).

Characteristics of the LC "Gluing" Statistical Copolymer. Polymeric LC patterns were studied by a quantitative birefringence imaging microscopy technique (Abrio). The magnitude of retardance and the azimuthal data are given for every image point. Different structural orientations are illustrated by means of different colors belonging each to a respective orientation, which is shown by the color wheel. A prerequisite of this quantitative assignment, a constant thickness of the polymer film, can be assumed for a polymer film between two glass plates at least on the submillimeter scale (checked by means of a profilometer, data not shown).[32] The Abrio images of the polymeric LC phase of PBOx-Chol-MPA in tetrahydrofuran (THF) obtained upon lateral shearing of the specimen in one direction reveal domains with the same color, thus the same structural orientation, on the length scale of tens to hundreds of micrometers (Figure 1).

Also, PBOx-Chol-MPA could be readily transferred into the sodium salt, by dialysis against 0.01 M NaOH, and dispersed into water within a few minutes of ultrasonication (the free acid PBOx-Chol-MPA could not be dispersed in water). Cryo-TEM analysis of a dispersion of 1 wt % PBOx-Chol-MPNa in 0.15 M saline solution revealed the presence of spherical aggregates with diameters of *ca.* 15−30 nm and worm-like aggregates with dimensions of *ca.* 15 × 3 nm^2 (Figure 2a). The worm-like aggregates possess a lamellar structuring with dark−bright−dark change (dark = hydrophilic side chains, bright = hydrophobic side chains), indicating the formation of disk-like "hamburger" micelles[113−115] or "hockey-puck" micelles[116] (Figure 2b).

Vanadium Pentoxide−LC "Gluing" Statistical Copolymer Composites. Vanadium pentoxide was synthesized according to Lagaly *et al.*[117] starting from ammonium metavanadate and hydrochloric acid (see Figure S3 in the SI: TEM image of V_2O_5 dried on a TEM grid). For synthesizing hybrid materials with defined amounts of V_2O_5, the V_2O_5 concentration was determined *via* freeze-drying neglecting residual, coordinated water (*ca.* 16% of water remained in the V_2O_5 sample after

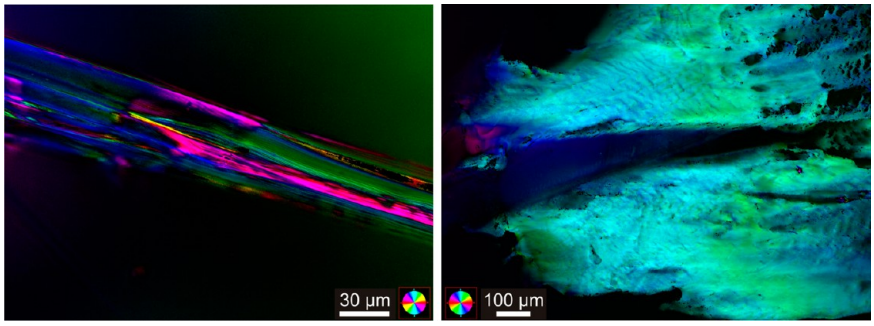

Figure 1. Quantitative birefringence optical micrograph (Abrio) images of shear-induced lyotropic phase formation of LC "gluing" copolymer 50+ wt % in THF.

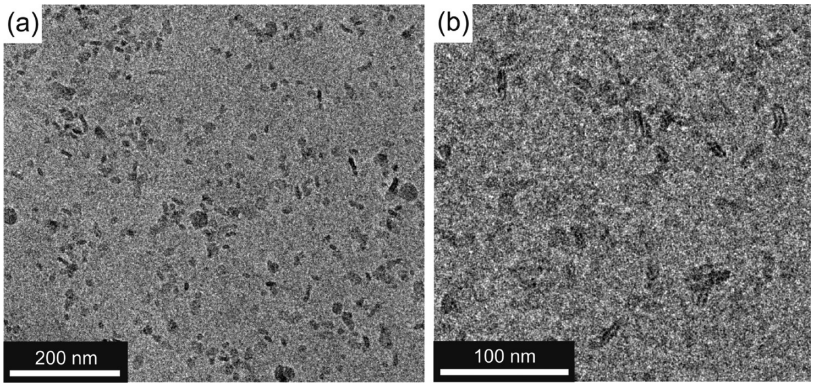

Figure 2. Cryo-TEM images of an aqueous dispersion of PBOx-Chol-MPNa under physiological conditions (polymer concentration: 10 mg mL^{-1}).

freeze-drying according to thermogravimetric analysis (TGA) (see Figure S4 in the SI)). The as-synthesized V_2O_5 tactosol was shaken vigorously to avoid the formation of preoriented V_2O_5 ribbons. After diluting the vanadium pentoxide tactosol to about 0.7 wt %[45] two different starting situations were used: the first starting point was an isotropic V_2O_5 mixture, and the second consisted of preoriented V_2O_5 building units in the tactoid sol that forms after 3−5 days when deposited in a closed vial without shaking. An analytical ultracentrifugation (AUC) sedimentation velocity experiment with a diluted isotropic V_2O_5 dispersion shaken continuously for about 4 weeks was performed to evaluate the size distribution of the dispersed species. The measurement reveals sizes of primary V_2O_5 ribbons mainly between 15 and 20 nm (assuming a spherical shape; see Figure S5 in the SI), which agrees with literature-reported results.[45] The sedimentation coefficient values taken from the resulting peak pattern of the V_2O_5 mixture (Figure S5) are always multiples of the sedimentation coefficient of primary V_2O_5 ribbons. This result suggests that formation of larger tactoids by shaking of the as-synthesized V_2O_5 dispersion can be avoided; however, up to *ca.* 7 V_2O_5 ribbons can assemble during shaking, probably *via* hydrogen bonding.[42] Notably, the bigger the size of the oligomeric V_2O_5 ribbons, the lower their total amount in the diluted tactosol, revealing that self-assembled ribbons are not preferably present within the tactosol, but upon xerogel or tactoid formation. When forming organic−inorganic hybrid materials by addition of an interacting polymer, repulsive forces, and consequently the distance, between V_2O_5 ribbons can be reduced. Herein, we used the LC "gluing" statistical copolymer PBOx-Chol-MPNa, in which the carboxylic acid side chains are able to adsorb to the oxygen-terminated face of V_2O_5 ribbons, like the acrylic/sulfonic copolymer (ACUSOL 588G) used by Lausser *et al.*[45] Since V_2O_5 is strongly negatively charged even at the pH of ∼4 of the aqueous mixture (negative electrophoretic mobility),[118] electrostatic binding of the polymer is not possible. However, binding *via* hydrogen bridges at the acidic pH on the oxygen-terminated faces involving the protonated carboxylic acid groups was the reported binding mode.[45] Upon addition of an aqueous dispersion of PBOx-Chol-MPNa while shaking slowly, formation of a reddish-brown precipitate was observed. The final mixture, exhibiting a pH of ∼4, was shaken overnight and purified first, by centrifugation at 1500 rpm (at this centrifugation speed sedimentation of nonbound polymer could be avoided), and second, by washing the reddish-brown precipitate with THF and thus dissolving and removing residual, nonbound polymer fractions. The composition of the V_2O_5−PBOx-Chol-MPNa hybrid materials formed was determined *via* TGA (see Figure S4 in the SI). Independent of the amount of polymer added (ratio

of V_2O_5:PBOx-Chol-MPNa of 1:1 and 2:1 w/w), the ratio of organic to inorganic part was found to be mainly dependent on the status of the diluted V_2O_5 tactosol. In the case of using an isotropic V_2O_5 dispersion the resulting hybrid materials contained ~57% V_2O_5 and ~33% polymer, and in the case of using a V_2O_5 tactoid, the composition of the hybrid material consisted of ~65% V_2O_5 and ~23% polymer (assuming a mass loss of the V_2O_5 fraction of 16% (see Figure S4 in the SI, V_2O_5 reference), probably deriving mainly from coordinated water at V_2O_5). The lower fraction of polymer when starting from preoriented V_2O_5 ribbons is probably due to the more limited accessibility of the oxygen-terminated crystal faces compared to an isotropic dispersion of V_2O_5.

Binding between V_2O_5 and LC polymer in aqueous dispersions consisting of V_2O_5 and LC polymer of 1:1 and 2:1 w/w was investigated in more detail *via* AUC sedimentation velocity experiments using absorption optics, aiming at quantifying the fraction of free V_2O_5 *vs* the fraction of V_2O_5 bound to polymer chains. For this purpose, a 0.1 wt % polymer dispersion was added slowly to a highly diluted dispersion of an isotropic V_2O_5 tactosol (0.005 wt %), exhibiting a final pH of ~4. Despite working with highly diluted V_2O_5 dispersions, precipitation was observed upon addition of polymer for both V_2O_5−polymer ratios, and in both cases the color of the supernatant changed from reddish-brown to yellowish, as already observed when adding polymer to higher concentrated V_2O_5 dispersions. AUC sedimentation velocity runs of both yellowish supernatants compared to a V_2O_5 reference sample (Figure S5 in the SI) reveal only the presence of nanosized species, probably ions or residual, nonbound polymer, indicative of quantitative binding of V_2O_5 to the polymer for both ratios (V_2O_5:polymer = 1:1 and 2:1 w/w, data not shown), resulting in rather defined species with sedimentation coefficients as multitudes of that for a single V_2O_5 ribbon. Both TGA results of the hybrid materials and AUC results of the supernatants indicate quantitative binding of V_2O_5 and polymer when using a ratio of V_2O_5:polymer = 2:1 w/w. Also, when using a ratio of V_2O_5 to polymer of 1:1 w/w, AUC analysis suggests that V_2O_5 also binds quantitatively to the polymer chains, but free polymer still remains in the reaction mixture. Only negligible amounts of V_2O_5 were found in the supernatants isolated after adding PBOx-Chol-MPNa to a V_2O_5 tactoid (V_2O_5:polymer = 1:1 and 2:1 w/w) *via* AUC analysis, assuming quantitative binding of V_2O_5 to the polymer. However, in contrast to starting the hybrid synthesis with an isotropic V_2O_5 mixture, TGA suggests that in both cases nonbound LC polymer remains in the reaction mixture.

Hierarchically Structured Organic−Inorganic Composite Materials Consisting of V_2O_5 and LC "Gluing" Statistical Copolymers. For the preparation of composite materials, phase transfer of the precipitate consisting of V_2O_5 and PBOx-Chol-MPNa isolated by centrifugation from aqueous media to THF was performed *via* two different methods. On one hand, the precipitate was freeze-dried and then swollen in THF. After removing excess THF and washing with THF, the composite material was rotationally sheared on alumina foil by means of a shear cell[32] using defined shear rates. On the other hand, phase transfer of the hybrid material was performed by redispersing the precipitate in THF after centrifugation and removing the supernatant. In order to remove as much water as possible, centrifugation and redispersion was repeated once. Then, analogous to the first method, the composite material was sheared *via* rotation on alumina foil by using a shear cell. An advantage of the method involving freeze-drying and swelling of the material is the higher control over concentration of the hybrid material in THF. Consequently, shearing of the composites was performed with composites possessing higher viscosity. In contrast to that, phase transfer *via* centrifugation enables complete dispersion of the hybrid material, and when completely dried, the centrifugation method leads finally to the formation of mechanically more stable composite materials compared to composites prepared *via* the freeze-drying/swelling phase-transfer method.

The so-formed V_2O_5−LC copolymer composite materials, prepared by adding a dispersion of LC copolymer PBOx-Chol-MPNa to a diluted V_2O_5 tactosol (isotropic mixture of V_2O_5 or V_2O_5 tactoid) resulting in composites with a ratio of V_2O_5 to polymer of ~2.8:1 w/w (when initiating the synthesis with a tactoid) or ~1.7:1 w/w (when initiating the synthesis using an isotropic mixture), were analyzed on the micro- to millimeter scale by quantitative birefringence imaging microscopy technique (Abrio), on the micrometer scale by scanning electron microscopy (SEM) and X-ray microtomography and on the micro- to nanometer scale by transmission electron microscopy (TEM) and small-angle X-ray scattering (SAXS). In the following, samples prepared by phase transfer *via* freeze-drying and swelling in THF are called **FD-TACT**, when started from a V_2O_5 tactoid, or **FD-ISO**, when started from an isotropic V_2O_5 dispersion, and *via* the centrifugation method **CEN-TACT**, when started from a V_2O_5 tactoid, and **CEN-ISO**, when started from an isotropic V_2O_5 dispersion.

Structuring on the Millimeter to Micrometer Length Scale. Abrio images of V_2O_5−LC copolymer composite materials **FD-TACT** and **FD-ISO** taken through longitudinal cuts parallel to the shearing direction (Figure 3a (**FD-TACT**) and b (**FD-ISO**), thickness of cuts 1 μm) and through cross sectional cuts perpendicular to the shearing direction (Figure 3c (**FD-TACT**) and d (**FD-ISO**), thickness of cuts 1 μm), reveal the formation of fibers that possess, depending on the orientation direction of the fiber, the same colors and, thus, the same structural orientations on the length scale of tens of micrometers, irrespective of whether a V_2O_5 tactoid

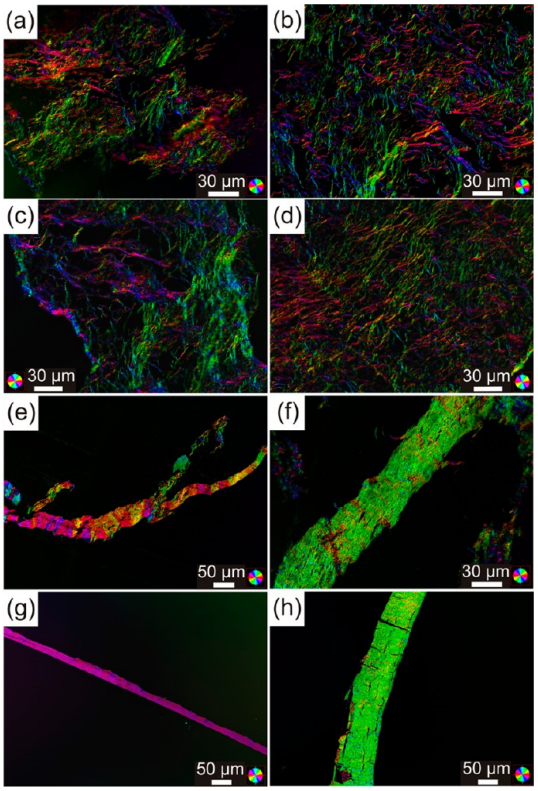

Figure 3. Quantitative birefringence optical micrograph (Abrio) images of V_2O_5–LC "gluing" statistical copolymer (PBOx-Chol-MPNa) composite materials starting from V_2O_5 tactoid (left column) or from isotropic V_2O_5 tactosol (right column). (a–d) Preparation of composites *via* phase transfer involving freeze-drying, followed by swelling in THF. Longitudinal cuts (thickness 1 μm) parallel to the shearing direction from composites FD-TACT (a) and FD-ISO (b); cross sectional cuts (thickness 1 μm) perpendicular to the shearing direction of composites FD-TACT (c) and FD-ISO (d). (e–h) Preparation of composites *via* phase transfer by centrifugation. Longitudinal cuts (thickness 1 μm) parallel to the shearing direction from composites CEN-TACT (e) and CEN-ISO (f); cross sectional cuts (thickness 0.5 μm) perpendicular to the shearing direction of composites CEN-TACT (g) and CEN-ISO (h).

or an isotropic V_2O_5 dispersion was used. Structures within the fibers itself seem to possess the same structural orientation. Fiber formation was likely induced by shearing the highly viscous swollen hybrid material.

V_2O_5–LC copolymer composite materials **CEN-TACT** and **CEN-ISO** formed *via* the centrifugation method were not fibrous on the micrometer length scale (Figure 3e–h). Abrio images of longitudinal sections (Figure 3e (**CEN-TACT**) and f (**CEN-ISO**), thickness of cuts 1 μm) show for both samples the formation of lyotropic regions with the same colors and hence the same structural orientations on the length scale of tens up to hundreds of micrometers. Abrio images of the cross sections of these samples (Figure 3g (**CEN-TACT**) and h (**CEN-ISO**), thickness of the cuts 0.5 μm) confirm observations from longitudinal sections and even reveal the formation of larger domains with the same structural orientation on the length scale of hundreds of micrometers for both V_2O_5 starting situations. These observations indicate that complete dispersion of V_2O_5 hybrid materials when performing the phase transfer *via* centrifugation compared to the phase-transfer method when freeze-drying and only swelling the material supports ordering of the structure on the length scale of tens up to hundreds of micrometers. In particular, starting the synthesis from the V_2O_5 tactoid and applying the centrifugation method leads to formation of composite materials with ordering on the length scale of hundreds of micrometers throughout the material. In addition, the density of the dried composites prepared *via* the centrifugation method seems to be higher than composites prepared *via* freeze-drying and swelling.

Structuring on the Micrometer Length Scale. An example cross sectional phase-contrast-enhanced radiograph of the composite **CEN-TACT** (Figure 4a) and a typical cross sectional virtual slice through the reconstructed volume (Figure 4b, inset bottom right) reveals a layered structuring, which was investigated in more detail by SEM. A typical longitudinal virtual slice through the reconstructed volume shows areas in the range of 100 $\times$ 100 μm^2 throughout the composite possessing a regular substructure with a texturing of *ca.* 5–6 μm as seen from the top view (Figure 4b). This is an additional hierarchical level of the composite on this length scale. A movie rendering of these data of **CEN-TACT** (thickness of 30–40 μm; see the SI) indicates that the texture is influenced by shearing and is more pronounced close to the force contact point.

SEM analysis revealed that the structures of composites obtained when performing the phase transfer *via* freeze-drying and subsequent swelling in THF seem to be built up of sheets on the lower micrometer scale (Figure 5a and b). These nanobelts and sheets build up the structures, which were observed on the micrometer scale in addition to the fibers (Figure 3a–d). However, the layered structuring of composites for which phase transfer was performed *via* centrifugation is much more pronounced, and the density of these layers in the dried composite materials is much higher (Figure 6a and b), matching the observations by phase-contrast-enhanced tomography. Alignment of V_2O_5 ribbons forming V_2O_5–LC polymer fibers finally building up layers within the composites prepared *via* both phase-transfer methods on the length scale of hundreds of nanometers was observed (Figure 5c and Figure 6c). Obviously, the complete dispersion of the hybrid material in THF when performing the phase transfer *via* centrifugation leads, after complete drying, to a dense composite material possessing a pronounced layered structuring on the length scale of few hundreds of nanometers, which is probably also

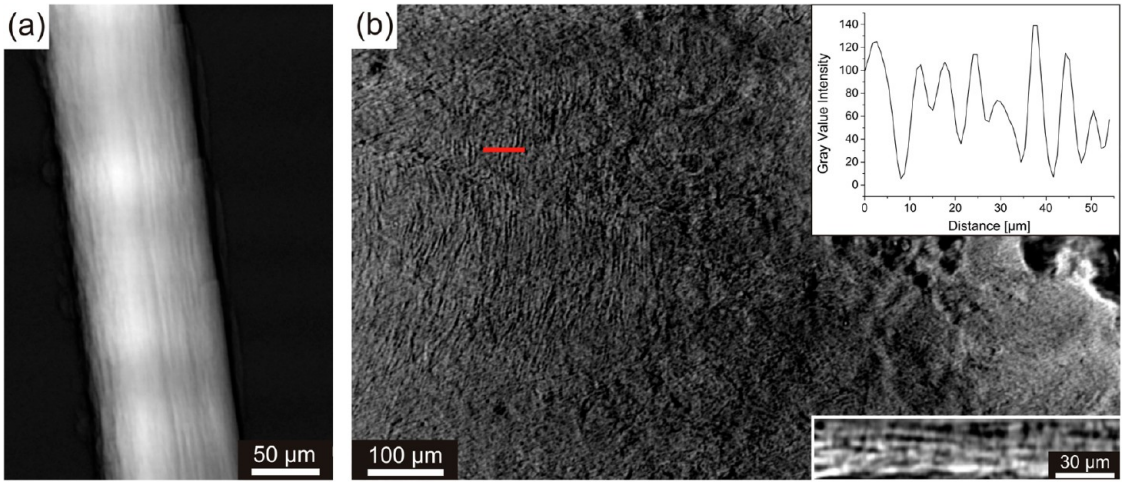

Figure 4. (a) Phase-contrast-enhanced monochromatic cross sectional radiograph and (b) a typical tomographic reconstruction slice of a longitudinal section and cross section (inset bottom right) of composite sample CEN-TACT. The inset diagram (top right) gray-level intensity *vs* distance reveals a regular texturing of *ca.* 5−6 μm over areas of 100 × 100 μm^2 in the longitudinal slice (the inset diagram plots intensity variations along the marked red line area).

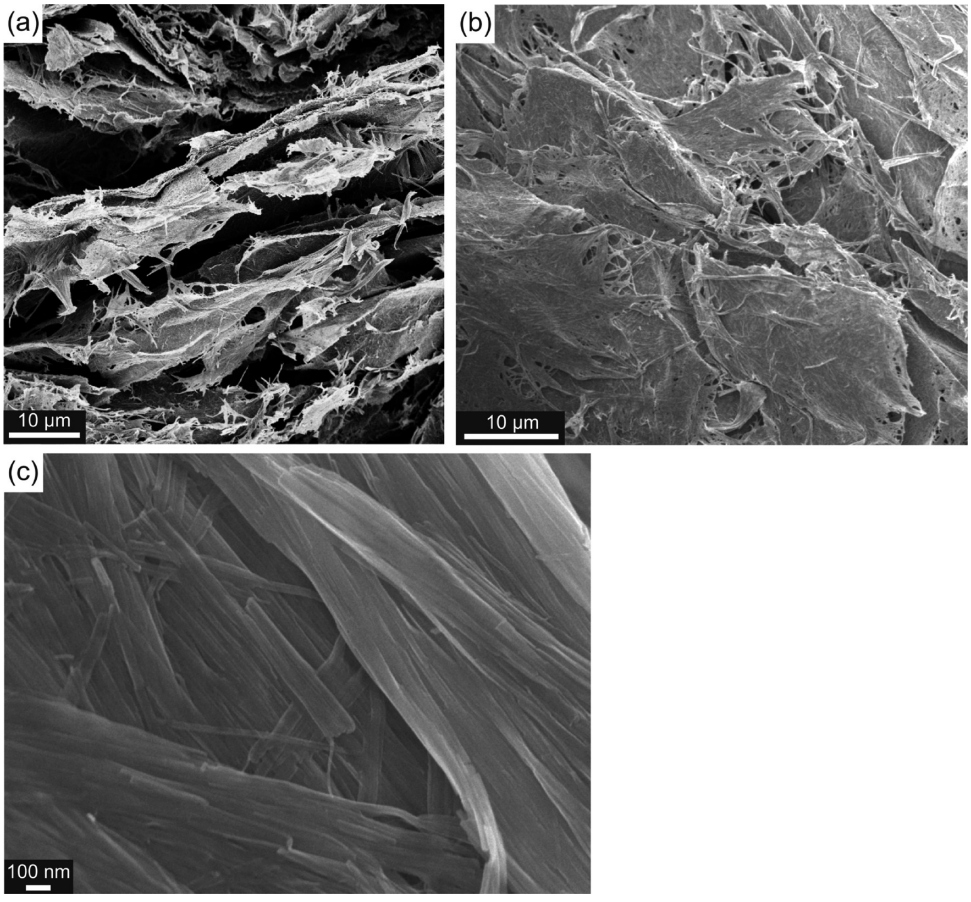

Figure 5. SEM analysis of cross section (a) and longitudinal sections (b, c) of V_2O_5 composite materials for which phase transfer was performed *via* freeze-drying and subsequent swelling in THF.

the reason that these composites are mechanically stable. In contrast to that, the fragility of the composites obtained after freeze-drying and swelling was so distinct that these materials were mechanically unstable, and thus, mechanical analysis was not possible.

Structuring on the Nanometer Length Scale. SAXS analysis and TEM analysis revealed of the nanostructure of the composites in more detail.

SAXS measurements were performed on all samples, for centrifugation and freeze-drying phase-transfer techniques and for tactosols with preoriented and

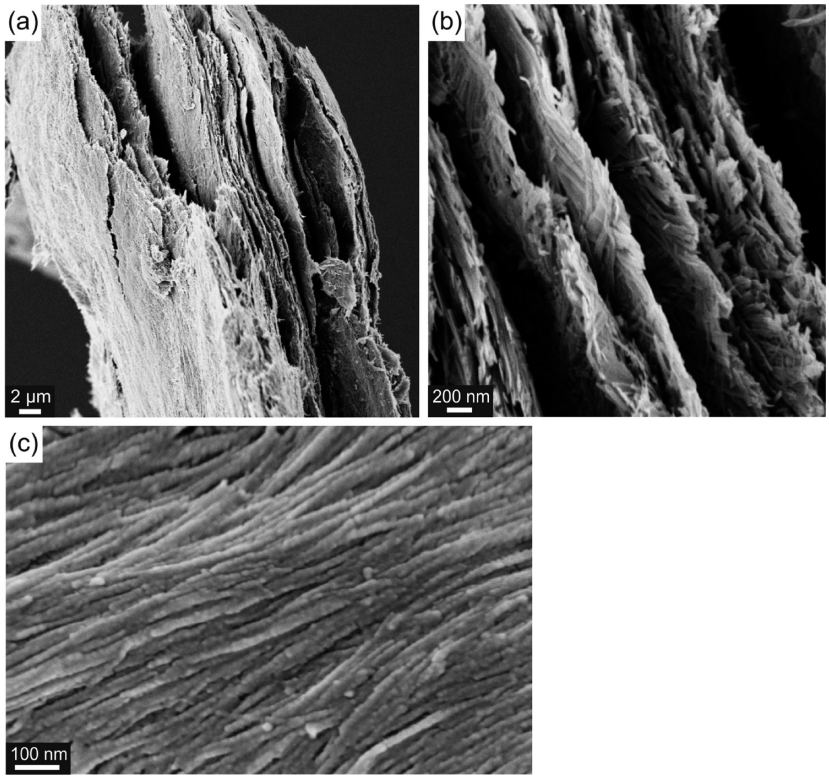

Figure 6. SEM analysis of the cross section (a and b) and longitudinal section (c) of V_2O_5 composite materials for which phase transfer was performed *via* centrifugation.

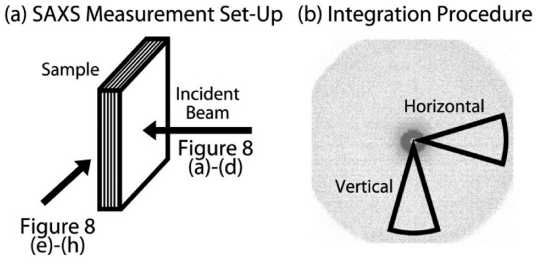

Figure 7. (a) Schematic representation of SAXS measurement setup. (b) Schematic representation of the intensity integration procedure.

isotropic V_2O_5 mixtures. The measurements were performed with the incident X-ray beam perpendicular and parallel to the layered structure as shown in Figure 7a. The 2D SAXS patterns for the incident beam perpendicular and parallel to the layered structure are presented in Figure 8a–d and Figure 8e–h, respectively. In addition, the intensity from Figure 8e–h was radially integrated to obtain detailed information on the packing and internal structure of V_2O_5. Due to obtained pattern anisotropy, the integration was performed in two distinct angular segments, ±20 degrees around the horizontal and vertical axes in the 2D patterns, as schematically shown in Figure 7b.

It can be seen that all SAXS 2D images combine a SAXS pattern appearing at the center and a diffraction peak corresponding to the V_2O_5 intersheet distance inside the ribbons (indicated in Figure 8a). In the samples in which phase transfer was performed *via* freeze-drying the isotropy of the SAXS patterns and the diffraction signals suggest that the V_2O_5 ribbons have no specific orientation when measuring perpendicular to the layered structure, as seen in Figure 8a (**FD-TACT**) and Figure 8c (**FD-ISO**). The slight anisotropy of the SAXS signal when measuring parallel to the layered structure indicates that the V_2O_5 ribbons are, to some extent, preferentially oriented parallel to the layers, Figure 8e (**FD-TACT**) and Figure 8g (**FD-ISO**). In addition, a diffraction peak with the intensity maximum coaligned with the SAXS signal indicates that the ribbons preferentially lie flat, parallel to the layers. On the other hand, in the samples in which phase transfer was performed *via* centrifugation, the lack of the diffraction peak when measuring perpendicular to the layered structure, Figure 8b (**CEN-TACT**) and Figure 8d (**CEN-ISO**), and the strong anisotropy of both SAXS and diffraction signals when measuring parallel to the layered structure, Figure 8f (**CEN-TACT**) and Figure 8h (**CEN-ISO**), suggest that most of the ribbons lie flat, parallel to the layers, exhibiting a highly ordered nanostructure.

As previously mentioned, in the samples prepared by freeze-drying, a diffraction peak is visible in both the horizontal and vertical integrations, when measuring parallel to the layered structure, Figure 8i and Figure 8k, at a Q of ~6.7 nm^{-1}. This value corresponds to a spacing of ~9.4 Å, which is in good agreement with previously reported V_2O_5 intersheet distance inside the

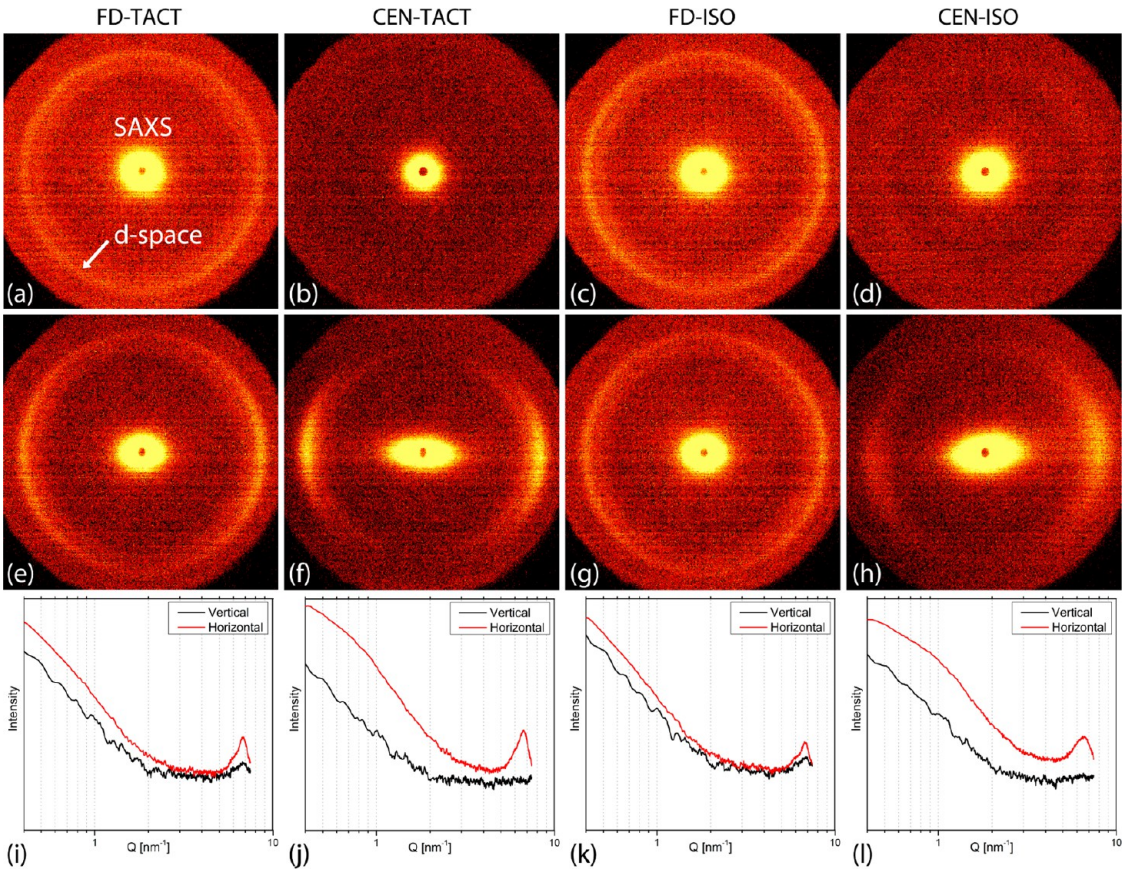

Figure 8. Representative SAXS data obtained from V_2O_5—LC "gluing" copolymer composites. (a—d) Patterns obtained with the incident beam perpendicular to the layered structure; (e—h) patterns obtained with the incident beam parallel to the layered structure: composite FD-TACT (patterns a and e), CEN-TACT (patterns b and f), FD-ISO (patterns c and g), and CEN-ISO (patterns d and h). (i—l) SAXS plots obtained by radial integration in the horizontal and vertical segments on 2D SAXS patterns obtained with the incident beam parallel to the layered structure.

ribbons of ~10.4 Å.[42] The difference in intersheet distances might result from phase transfer from water to THF and, thus, from drastically decreasing the amount of water inside the ribbons.[39,42]

In the samples prepared by centrifugation, a strong diffraction peak, at a similar Q value of ~6.7 nm^{-1}, is evident only in horizontal integration, Figure 8j and l. In addition, a shoulder at Q of ~0.8 nm^{-1} and ~1 nm^{-1} nm appears in the horizontal integration of preoriented and isotropic samples, respectively, which may suggest a close packing of V_2O_5 ribbons with an average thickness of ~7.8 and ~6.3 nm, respectively, into fibers that lie flat parallel to the sample surface. Thicker ribbons are probably the result of preorientation of the tactosol. These observations support the conclusion that the samples in which phase transfer was performed *via* the centrifugation method exhibit a highly ordered and anisotropic nanostructure. It is worth mentioning that a small shoulder also appears at a Q of ~5.9 nm^{-1}, near the main diffraction peak, corresponding to a spacing of ~10.6 Å. Although the source of the peak is not completely understood, it may suggest the existence of two distinct populations of V_2O_5 ribbons with different intersheet distances: a bigger population probably corresponding to the already above-mentioned intersheet distance of 9.4 Å (the main structural feature) and a smaller population that can be assigned to a bigger intersheet distance (a minor structural feature), which is obviously a result of different amounts of intercalated water, independent of the amount of polymer added.

Longitudinal and cross sections of all V_2O_5—LC polymer composites were visualized by TEM. All specimens, cross section (thickness of 85 nm), and longitudinal section (thickness of 95 nm) of composites **FD-ISO** (Figure 9a and b, respectively) and **FD-TACT** (Figure 9c and d, respectively) prepared *via* phase transfer by freeze-drying and swelling in THF reveal domains of coaligned fibrous-like structures. Alignment, however, was only observed in domains on the lower tens of nanometers scale, whereas on the higher scale the microstructures do not show any specific orientation in both directions, confirming observations obtained by SEM and SAXS analysis. Images of cross sections and longitudinal sections of both samples, **FD-ISO** and **FD-TACT**, look very similar (Figure 9), suggesting that the obtained structures are independent of starting the hybrid synthesis from an isotropic

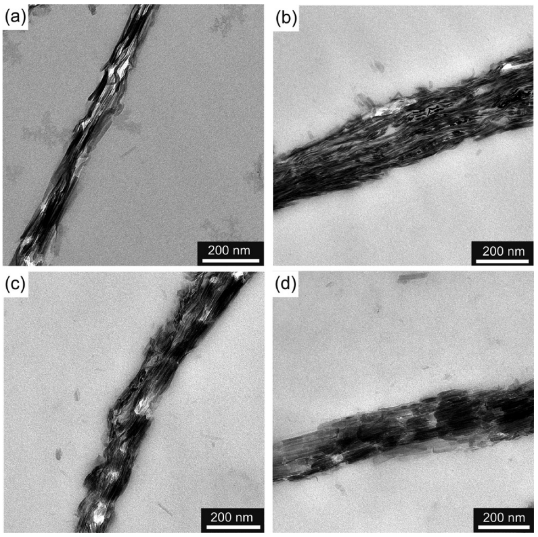

Figure 9. TEM images of composite materials obtained from LC "gluing" copolymer and isotropic V_2O_5 tactosol (FD-ISO; (a) cross section and (b) longitudinal section) or V_2O_5 tactoid (FD-TACT; (c) cross section and (d) longitudinal section). Phase transfer from aqueous medium to THF was performed *via* freeze-drying and swelling in THF, followed by rotational shearing of the samples. Cross sectional cuts of the composites exhibit a thickness of 85 nm and longitudinal cuts a thickness of 95 nm.

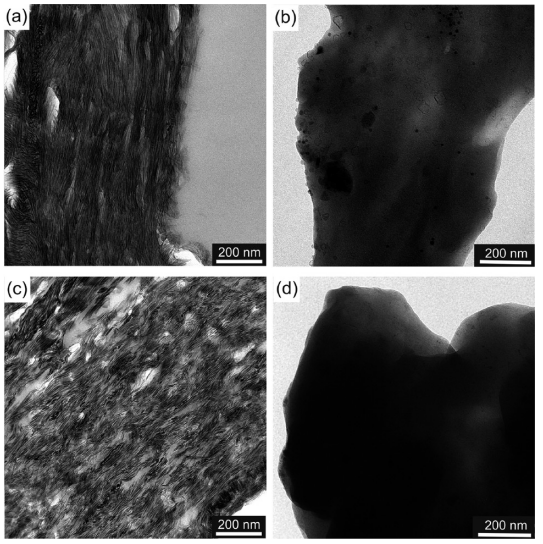

Figure 10. TEM images of composite materials obtained from LC "gluing" copolymer and isotropic V_2O_5 tactosol (CEN-ISO; (a) cross section and (b) longitudinal section) or V_2O_5 tactoid (CEN-TACT; (c) cross section and (d) longitudinal section). Phase transfer from aqueous medium to THF was performed *via* centrifugation, and subsequently, samples were rotationally sheared. Cross sectional cuts of the composites exhibit a thickness of 85 nm and longitudinal cuts a thickness of 95 nm.

V_2O_5 dispersion or a tactoid. BET measurements on composite material **FD-ISO** revealed a surface area of 33 m^2/g. This result and the curve progression of the isotherm (data not shown) are consistent with the microstructure observed *via* SEM. The surface is a microstructured system of nanopores, probably filled with the polymer.

Cross section (thickness of 85 nm) and longitudinal section (thickness of 95 nm) of composites **CEN-ISO** (Figure 10a and b, respectively) and **CEN-TACT** (Figure 10c and d, respectively) prepared *via* phase transfer by centrifugation reveal the anisotropy observed by both SEM and SAXS analysis. While the cross sections of the samples (Figure 10a and c) show densely packed fibrous-like structures coaligned on the length scale of a few hundreds of nanometers, the longitudinal cuts (Figure 10b and d) reveal no internal structure. FFT analysis of the cross sections **CEN-ISO** and **CEN-TACT** further supports the superstructure of packed V_2O_5 fibers in a size range previously obtained by SAXS analysis (Figure S6, in the SI). Electron diffraction of the cross sections revealed spots corresponding to a distance of *ca.* 8.3 Å assigned to the intersheet distance inside the ribbons (deviations of distances measured by SAXS are probably due to the calibration standard of the TEM instrument). The spots were observed only when measuring cross sections of the samples (Figure S7 in the SI), further confirming the anisotropic nature of V_2O_5 and thus a highly ordered composite nanostructure for both composite samples **CEN-TACT** and **CEN-ISO**.

A comparison of the results obtained on the micrometer to nanometer length scale *via* SEM, TEM, and SAXS analysis reveals the superiority of the phase-transfer method *via* centrifugation over the method involving freeze-drying and swelling in THF. By completely dispersing the hybrid materials when performing the phase transfer *via* centrifugation, a very compact microstructure and highly defined nanostructure of the composites **CEN-TACT** and **CEN-ISO** were obtained, independent of initiating the synthesis with an isotropic V_2O_5 tactosol or a V_2O_5 tactoid. The high mutual order of V_2O_5 ribbons within the V_2O_5–LC polymer fibers suggests the formation of mesocrystalline arrangements. Abrio analysis of this composite material reveals long-range orientation on the length scale of hundreds of micrometers consisting of stacked V_2O_5 ribbons within a chiral nematic polymer matrix, finally forming the layered structuring on the nano- to micrometer length scale in the horizontal dimension and the textured substructure on the lower micrometer length scale in the vertical dimension.

Mechanical Analysis. Mechanical characterization was performed by the nanoindentation technique only on samples for which phase transfer was performed *via* centrifugation, as the composites for which phase transfer was performed *via* freeze-drying were mechanically unstable. Measurements were performed on polished samples parallel and perpendicular to the layered structure, on a cross section, and on the surface of the sample, respectively. Reduced moduli of composites prepared from isotropic and preoriented mixtures are summarized in Table 1. For comparison, nanoindentation was also performed on pure polymer material and pure V_2O_5.

First, it is evident that the reduced modulus of pure polymer is relatively low, at 0.9 GPa. In comparison, the reduced modulus of pure V_2O_5 is relatively high, with values of 21.2 and 28.9 GPa for isotropic and preoriented mixtures, respectively. This result is in good agreement with the previously reported reduced modulus of 24 GPa measured by tensile tests.[42] The obtained reduced moduli of 17.25 and 17.4 GPa and hardness of 0.5 GPa measured on the cross sections of the hierarchically structured V_2O_5—polymer composites are comparable to nanoindentation properties of inorganic—organic hierarchically structured biocomposites such as human bone and dentin. In human cortical bone an average reduced modulus of *ca.* 17.4 GPa and a hardness of *ca.* 0.52 GPa (both values for osteons) were reported.[119] In intertubular dentin a reduced modulus in the range 17.7 (near the pulp) to 21.1 GPa (near the enamel) and a hardness of about 0.5 GPa were found.[120,121]

Anisotropy in mechanical properties measured in V_2O_5 composite confirms the obtained structural anisotropy. Reduced modulus values obtained on the cross section, 17.25 and 17.4 GPa, for isotropic and preoriented composites, respectively, are lower than the values obtained in pure V_2O_5 due to the presence of the compliant organic phase. The reduced modulus measured on the surface is approximately two times lower than the modulus obtained when indenting the cross section of the specimen, but is still significantly higher than the properties of the pure polymer.

TABLE 1. Average Reduced Modulus of V_2O_5 Composites, for Which Phase Transfer Was Performed *via* Centrifugation, and Pure Constituents

	reduced modulus [GPa]
Pure Polymer	0.9 (0.02)
Pure V_2O_5	
isotropic	21.2 (4.3)
preoriented	28.9 (5.1)
V_2O_5 Composites	
Cross Section	
isotropic	17.25 (1.9)
preoriented	17.4 (1.4)
Surface	
isotropic	9.8 (1.0)
preoriented	8.4 (1.7)

CONCLUSION

Hierarchically structured V_2O_5—LC "gluing" polymer composite materials were fabricated *via* a one-step self-assembly forming six hierarchical levels driven by liquid crystal formation (Scheme 3). The assembly of V_2O_5 sheets to V_2O_5 ribbons forms the first hierarchical level. The LC "gluing" statistical copolymer functionalized with pendant cholesteryl and carboxyl side chains binds to the ribbons *via* the carboxyl units ("gluing units"), forming the glue between organic and inorganic components. The polymeric chiral nematic LC phase is induced by the cholesteryl side chains that form the second and third hierarchical level, and long-range orientation of the polymeric phase is achieved by shearing. The formed V_2O_5—polymer fibers consisting of V_2O_5 ribbons with LC polymer in between lay flat and parallel to the surface (fourth level), finally forming a layered composite structure in the horizontal dimension (fifth level) and a textured substructure in the vertical dimension (sixth level).

The structure of dried composites, investigated from the millimeter and micrometer to the nanometer length scale by means of light microscopy, phase contrast-enhanced microtomography, SEM, TEM, and SAXS is strongly influenced by the preparation method: Two different starting situations from the V_2O_5 tactosol were chosen (isotropic mixture and V_2O_5 tactoid), and phase transfer from aqueous medium to THF, in which the LC polymer was found to form lyotropic phases with the same orientation up to hundreds of micrometers upon shearing, was performed by either freeze-drying and subsequent swelling or centrifugation and redispersion. Structures

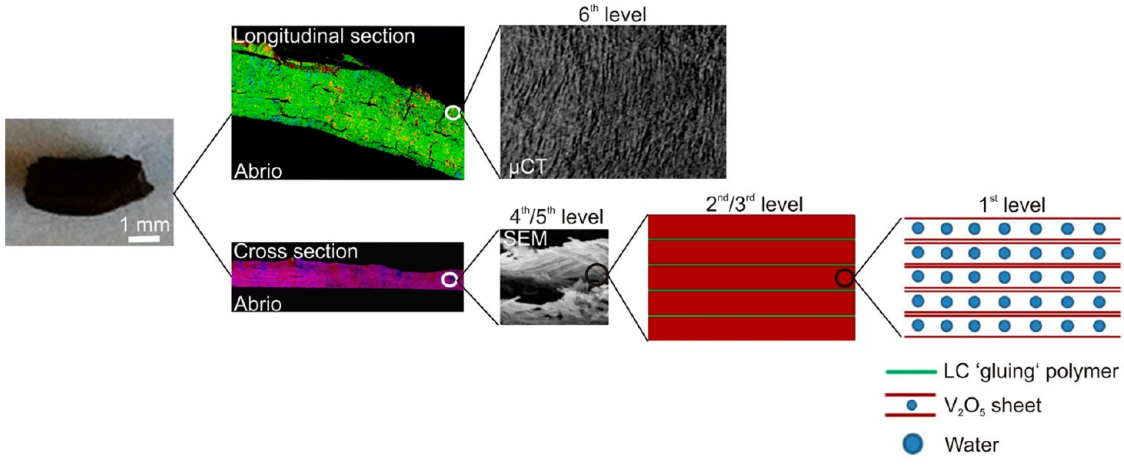

Scheme 3. Illustration of hierarchically structured V_2O_5—LC polymer composite materials.

exhibiting the highest ordering from the milli- and micrometer down to the nanometer length scale finally forming mesocrystalline arrangements were obtained when performing the phase transfer *via* the centrifugation method, even when starting the hybrid synthesis from isotropic V_2O_5 dispersions.

Mechanical analysis by nanoindentation matches the structural anisotropy and also reveals that the reduced modulus of the composites was decreased by adding more compliant phase compared to the reduced modulus of pure V_2O_5. Since vanadia is a functional material with interesting properties, *e.g.*, in catalysis, redox chemistry, and electrochromism, the synthesized composites show great promise for other potential functions in addition to mechanical reinforcement.

MATERIALS AND METHODS

Chemicals and Materials. Chemicals and solvents were purchased from several suppliers and used as received. Aldrich: 2-chloroethylamine hydrochloride (99%), *N*-hydroxysuccinimide (98%), 3-mercaptopropionic acid, methyl triflate (99%), thiocholesterol, 4-pentenoic acid, ammonium metavanadate (≥99.5%). Iris-Biotech: 1-(3-dimethylpropyl)-3-ethylcarbodiimide hydrochloride (99.4%). 2-(3-Butenyl)-2-oxazoline was synthesized starting from 4-pentenoic acid as described earlier.[122]

Analytical Instrumentation and Methods. ^{1}H NMR measurements were carried out at room temperature using a Bruker Avance III 400 operating at 400 MHz. $CDCl_3$ (purchased from Deutero GmbH, Germany) was used as solvent, and signals were referenced to $\delta = 7.26$ ppm. TGA (Netzsch TG 209 F1) was performed by heating the respective sample from room temperature to 1000 °C with a heating rate of 10 K/min under nitrogen. Analytical ultracentrifugation was performed on an Optima XL-I ultracentrifuge (Beckman Coulter, Palo Alto, CA, USA) in 12 mm Ti-double sector centerpieces (Nanolytics, Potsdam, Germany) at 25 °C using UV/vis absorption optics at 275 nm. Gel permeation chromatography (GPC) measurement was performed on a PL GPC 50 by using THF (stabilized with 0.0125% BHT) as eluent at 40 °C with a flow rate of 1 mL/min, and MALDI-ToF MS measurement was performed on a Bruker Microflex MALDI-TOF by using 10 μL of polymer precursor solution (10 mg/mL in $CHCl_3$), a 10 μL solution of dithranol (10 mg/mL in acetone), and 1 μL of sodium trifluoroacetate (0.1 mg/mL in acetone). Light micrographs were taken in transmission mode with a Zeiss Axio Imager.M2m microscope and a birefringence microscope (Abrio, Cambridge Research & Instrumentation, Inc. CRi, MA, USA). TEM images were recorded on a Zeiss Libra 120 microscope operating at 120 kV. TEM samples as well as samples for Abrio measurements were embedded in Spurr resin and cured at 60 °C, and thin microtome slices were obtained with a Reichert Ultracut S microtome. Cryo-TEM measurements of aqueous polymer dispersions with a concentration 10 mg/mL were performed on lacey carbon grids. After vitrifying by quickly plunging the grids into liquid ethane at its freezing point, the polymer samples were investigated at *ca.* 90 K. The obtained images were processed by using a background-subtraction routine, and if needed, a smoothing filter was used in order to reduce noise. Nitrogen (N_2) adsorption/desorption experiments were carried out with a Quadrasorb-MP machine (Quantachrome Instruments, Boynton Beach, FL, USA) at liquid nitrogen temperature (77.4 K). Initial data analysis was performed using the QuadraWin 5.05 software package (also Quantachrome Instruments). The surface area was calculated by using the Brunauer–Emmett–Teller (BET) equation. Phase-contrast-enhanced microtomography was obtained and reconstructed by combining methods previously published.[32,123] The relatively thin plate-shaped (high surface-to-volume ratio) samples with low absorption and intricate density variations proved challenging to image by X-ray, making it necessary to combine several tomographic scans employing propagation-based imaging in a partial-coherent synchrotron radiation facility (BAMline CT setup, Bessy II of the Helmholtz-Zentrum Berlin für Materialien and Energie (HZB)).[124] We therefore used image correlation to align three scans (as reported elsewhere[123]) each with 1800 projections obtained by on-axis half-circle rotation. The samples were imaged upright using an energy of 15 keV with an effective pixel size of 0.876 μm using a Fresnel propagation contrast-enhancement distance of 25 mm (between the sample and the imaging system). Normalized images from the three scans were coaligned, averaged, and reconstructed using commercial software (Bruker-CT, Kontich, Belgium, Nrecon 1.6.9.4). NIH Imagej[125] and CTvox (v 2.6, Bruker-CT, Kontich, Belgium) were used for visualization and analysis. SEM measurements were sputtered with gold on a Zeiss CrossBeam 1540XB. SAXS measurements were carried out using a NanoSTAR diffractometer (Bruker AXS GmbH, Karlsruhe, Germany) with a Cu Kα X-ray source and two crossed Goebel mirrors resulting in a wavelength of 0.154 nm and a beam size of approximately 400 μm in diameter. The Bruker Hi-STAR area detector was mounted at a distance of 1050 or 260 mm from the sample, which was later calibrated using crystalline silver behenate powder. The intensity was determined as a function of the scattering vector q and corrected for background and dark current. Nanoindentation was performed using a Triboindenter TI950 nanoindenter (Hysitron, Minneapolis, MN, USA), using a Berkovich tip. Samples were embedded in PMMA and polished in the desired direction. The load function was set to a loading/unloading rate of 100 μN/s with a holding time at peak load of 500 μN for 30 s. Data were collected in open-loop mode with 1026 points per indent. Load–displacement curves were analyzed for reduced modulus and hardness according to the Oliver and Pharr method.[126]

Synthesis of Poly[2-(3-butenyl)-2-oxazoline]. The microwave-assisted polymerization of 2-(3-butenyl)-2-oxazoline (BOx) was conducted at 140 °C as described by Schubert *et al.*[127] The reactions were carried out in dry acetonitrile (freshly distilled from CaH_2) under a dry argon atmosphere using methyl triflate (MeTf) as the initiator ($[BOx]_0 = 3$ M, $[MeTf]_0 \approx 0.03$ M); reaction time was 20 min. After completion of the reaction, the polymerization was terminated by the addition of 3 equiv of piperidine at room temperature and stirring for another 5 h at 70 °C. The reaction mixture was dialyzed against methanol (MWCO: 1 kDa) for 3 d. Evaporation of the solvent and freeze-drying from benzene afforded poly[2-(3-butenyl)-2-oxazoline] (PBOx), yield: 91% (3.68 g). ^{1}H NMR (400 MHz, $CDCl_3$): δ 1.10–1.43 (m, 0.04H), 2.03 (m, 0.01H), 2.34–2.43 (m, 4.05H), 2.95–3.02 (m, 0.02H), 3.45 (bs, 4.03H), 4.98–5.07 (m, 2.03H), 5.79–5.84 (m, 1H). MALDI-ToF MS (dithranol, Na^+): $M_n = 7.2$ kg mol^{-1}. GPC (THF; PS calibration): $M_n^{app} = 7.6$ kg mol^{-1}, $M_w^{app} = 8.4$ kg mol^{-1}.

Synthesis of Statistical LC "Gluing" Copolymer. Thiocholesterol (49.2 mg, 0.13 mmol) and 3-mercaptopropionic acid (13.5 mg, 0.13 mol) were added to a solution of PBOx (51 mg, 0.4 mmol C=C) in dry THF (1.5 mL). The reaction mixture was degassed three times, put under an argon atmosphere, and exposed to UV light (source: Heraeus TQ 150) at room temperature for 24 h. After exhaustive dialysis of the reaction mixture against THF and ethanol (MWCO: 1 kDa), the solvent was evaporated to dryness, and the residual solid was freeze-dried from benzene (gravimetric yield: 104.5 mg, >95%). ^{1}H NMR (400 MHz, $CDCl_3$): δ 0.6–2.7, 2.75 (br, SCH_2 MPA), 3.3–3.6 (br, NCH_2 backbone), 4.9–5.1 (m, =CH_2 BOx), 5.5 (s, =CH– Chol), 5.8–5.9 (–CH= BOx) (see ^{1}H NMR spectrum, Figure S2 in the SI).

Composite Materials Consisting of V_2O_5 and LC "Gluing" Copolymers. The V_2O_5 tactosol was synthesized according to Lagaly *et al.*[117] The V_2O_5 tactosol was diluted with Milli-Q water according to Lausser *et al.*,[45] finally obtaining a concentration of *ca.* 0.7 wt %

(neglecting the amount of coordinated water at V_2O_5 remaining after freeze-drying). Two different starting situations of the V_2O_5 tactosol for the synthesis of organic–inorganic hybrid materials were used: first, an isotropic V_2O_5 dispersion, and second, a V_2O_5 tactoid consisting of preoriented V_2O_5 ribbons formed after at least 3–5 days when deposited in a closed vial without shaking (indicated by a phase separation). For both approaches, preparation of hybrid materials in aqueous medium was similar. While slowly shaking the diluted V_2O_5 tactosol, an aqueous dispersion of LC polymer (c = 1 mg mL^{-1} when working with isotropic V_2O_5 dispersions and c = 2.5 mg mL^{-1} when working with V_2O_5 tactoids) was added in a ratio of V_2O_5 to LC copolymer of 2:1 (w/w) (neglecting the amount of coordinated water at V_2O_5 remaining after freeze-drying). Upon addition of the polymer dispersion, a reddish-brown precipitate formed, and the reaction mixture was shaken for 24 h, allowing the polymer to bind to V_2O_5. The yellow supernatant was removed, and the precipitate was isolated by centrifugation (1500 rpm, 5 min). After washing the precipitate with 3 mL of water and isolating the precipitate by a second centrifugation step (1500 rpm, 5 min), two different methods for the phase transfer from aqueous medium to THF were performed. In the first method, the precipitate was freeze-dried and subsequently swollen in THF for *ca.* 2 h. After removing excess THF, the composite was put onto an alumina foil and rotationally sheared by means of a shear cell. In the second method, phase transfer was carried out by dispersing the precipitate in THF and isolating the precipitate by centrifugation (1500 rpm, 5 min). After repeating this step to remove as much water as possible, the precipitate was centrifuged again at 5000 rpm for 5 min, finally obtaining a viscous, reddish composite material, which was transferred onto an alumina foil and rotationally sheared by means of a shear cell.

The shear cell consisting of a motor-driven disk (driven motor was purchased from Conrad: Getriebemotor 3000:1 4.5–15 V 540er Motor) and a distance holder enables constant rotational shearing forces by applying a constant rotation speed of 680° per minute clockwise and by using a distance holder of 0.4, 0.5, or 1.5 mm (depending on the desired final size of the composite). After pressing the motor-driven disk against the distance holder with the viscous hybrid material in its center by exerting normal forces in the range *ca.* 1–3 N and after shearing the material, the disk was lifted, allowing the solvent to evaporate.

The composition of V_2O_5–LC polymer hybrid materials was investigated by TGA and AUC sedimentation velocity experiments starting the synthesis with V_2O_5/polymer ratios of 1:1 and 2:1 w/w as well as using V_2O_5 tactoid and isotropic V_2O_5 dispersions as a starting point. TGA samples were prepared analogously to the composite samples *via* the phase transfer by freeze-drying and swelling in THF; however, instead of shearing and drying the sample at room temperature, the respective hybrid material was dried under vacuum. LC "gluing" polymer and V_2O_5 references were freeze-dried prior to TGA analysis. For AUC sedimentation velocity experiments hybrid materials starting from an isotropic dispersion were prepared by diluting an isotropic V_2O_5 tactosol to 0.005 wt % (pH ~4) and adding the respective amount of LC polymer dispersion (c = 1 mg/mL), followed by shaking the mixture overnight. In the case of starting the synthesis from V_2O_5 tactoids (*ca.* 0.7 wt %), the respective amount of polymer dispersion was added and the mixture shaken overnight. After dilution, the dispersions exhibited a pH of ~4–5. In all dispersions precipitated hybrid particles were separated from the supernatant solution, and AUC measurements were performed with all yellow supernatants to quantify the amount of V_2O_5 that did not bind to the polymer and form hybrid materials.

Conflict of Interest: The authors declare no competing financial interest.

Acknowledgment. We thank the German Research Foundation DFG through the Priority Programme 1420 'Biomimetic Materials Research: Functionality by Hierarchical Structuring of Materials' for financial support. P.Z. is also grateful to the Berlin-Brandenburg Center for Regenerative Therapies (BCRT) for financial support. We thank Dr. Elena Rosseeva for help with electron diffraction analyses, Rose Rosenberg for AUC measurements, Lauretta Nejedli for microtome cuts for TEM analysis and cuts for light micrograph measurements, the Proteomics Center (Konstanz), especially Dr. Andreas Marquardt, for MALDI-ToF MS measurements, Ingrid Zenke for assistance in SAXS measurements, Dr. Markus Drechsler for cryoTEM measurements, Dr. Jens Weber for BET measurements, Lars Bolk for GPC analysis, and Ursula Lubahn for TGA analysis. We thank HZB for the allocation of synchrotron radiation beam time and excellent technical support of the BAM staff H. Riesermeier, R. Britzke, T. Wolk, and B. Mueller.

Supporting Information Available: MALDI-ToF mass spectrum of poly[2-(3-butenyl)oxazoline], ^{1}H NMR spectrum of statistical LC "gluing" polymer, TGA data of hybrid materials, V_2O_5 reference and polymer reference, AUC sedimentation coefficient distribution of V_2O_5 dispersion, TEM data of V_2O_5 reference and microtome cuts of V_2O_5–LC polymer composite samples, as well as a video rendering the data of the tomographically reconstructed volume of composite **CEN-TACT** from bottom to top. This material is available free of charge *via* the Internet at http://pubs.acs.org.

REFERENCES AND NOTES

1. Meldrum, F. C.; Cölfen, H. Controlling Mineral Morphologies and Structures in Biological and Synthetic Systems. *Chem. Rev.* **2008**, *108*, 4332–4432.
2. Lowenstam, H. A.; Weiner, S. *On Biomineralization*; Oxford University Press: New York, 1989.
3. Meyers, M. A.; McKittrick, J.; Chen, P.-Y. Structural Biological Materials: Critical Mechanics-Materials Connections. *Science* **2013**, *339*, 773–779.
4. Aichmayer, B.; Fratzl, P. Vielseitige Biominerale - Wie aus Brüchigen Mineralen Hochwertige Verbundmaterialien Entstehen. *Phys. J.* **2010**, *9*, 33–38.
5. Fratzl, P.; Weinkamer, R. Nature's Hierarchical Materials. *Prog. Mater. Sci.* **2007**, *52*, 1263–1334.
6. Ritchie, R. O. The Conflicts between Strength and Toughness. *Nat. Mater.* **2011**, *10*, 817–822.
7. Oaki, Y.; Imai, H. The Hierarchical Architecture of Nacre and Its Mimetic Material. *Angew. Chem., Int. Ed.* **2005**, *44*, 6571–6575.
8. Xie, L.; Wang, X.-X.; Li, J. The SEM and TEM Study on the Laminated Structure of Individual Aragonitic Nacre Tablet in Freshwater Bivalve H. cumingii Lea Shell. *J. Struct. Biol.* **2010**, *169*, 89–94.
9. Jäger, I.; Fratzl, P. Mineralized Collagen Fibrils: A Mechanical Model with a Staggered Arrangement of Mineral Particles. *Biophys. J.* **2000**, *79*, 1737–1746.
10. Lin, A. Y.-M.; Meyers, M. A. Interfacial Shear Strength in Abalone Nacre. *J. Mech. Behav. Biomed. Mater.* **2009**, *2*, 607–612.
11. Meyers, M. A.; Lin, A. Y.-M.; Chen, P.-Y.; Muyco, J. Mechanical Strength of Abalone Nacre: Role of the Soft Organic Layer. *J. Mech. Behav. Biomed. Mater.* **2008**, *1*, 76–85.
12. Bezares, J.; Asaro, R. J.; Hawley, M. Macromolecular Structure of the Organic Framework of Nacre in Haliotis Rufescens: Implications for Mechanical Response. *J. Struct. Biol.* **2010**, *170*, 484–500.
13. Gries, K.; Kröger, R.; Kübel, C.; Schowalter, M.; Fritz, M.; Rosenauer, A. Correlation of the Orientation of Stacked Aragonite Platelets in Nacre and Their Connection via Mineral Bridges. *Ultramicroscopy* **2009**, *109*, 230–236.
14. Mohanty, B.; Katti, K. S.; Katti, D. R. Experimental Investigation of Nanomechanics of the Mineral-Protein Interface in Nacre. *Mech. Res. Commun.* **2008**, *35*, 17–23.
15. Schäffer, T. E.; Ionescu-Zanetti, C.; Proksch, R.; Fritz, M.; Walters, D. A.; Almqvist, N.; Zaremba, C. M.; Belcher, A. M.; Smith, B. L.; Stucky, G. D.; *et al*. Does Abalone Nacre Form by Heteroepitaxial Nucleation or by Growth through Mineral Bridges? *Chem. Mater.* **1997**, *9*, 1731–1740.
16. Fratzl, P.; Burgert, I.; Gupta, H. S. On the Role of Interface Polymers for the Mechanics of Natural Polymeric Composites. *Phys. Chem. Chem. Phys.* **2004**, *6*, 5575–5579.
17. Chepikov, A. M.; Minenko, S. S.; Lisetski, L. N.; Levovka, N. I.; Usol'tseva, N. V.; Soskin, M. S. Dispersions of Carbon

Nanotubes and Organomodified Clay Platelets in Cholesteric Liquid Crystals. *Funct. Mater.* **2012**, *19*, 343–347.
18. Tang, Z.; Kotov, N. A.; Magonov, S.; Ozturk, B. Nanostructured Artificial Nacre. *Nat. Mater.* **2003**, *2*, 413–418.
19. Podsiadlo, P.; Liu, Z.; Paterson, D.; Messersmith, P. B.; Kotov, N. A. Fusion of Seashell Nacre and Marine Bioadhesive Analogs: High-Strength Nanocomposite by Layer-by-Layer Assembly of Clay and L-3,4-Dihydroxyphenylalanine Polymer. *Adv. Mater.* **2007**, *19*, 949–955.
20. Yeom, B.; Suhan, K.; Jinhan, C.; Junhee, H.; Kookheon, C. Effect of Interfacial Adhesion on the Mechanical Properties of Organic/Inorganic Hybrid Nanolaminates. *J. Adhes.* **2006**, *82*, 447–468.
21. Finnemore, A.; Cunha, P.; Shean, T.; Vignolini, S.; Guldin, S.; Oyen, M.; Steiner, U. Biomimetic Layer-by-Layer Assembly of Artificial Nacre. *Nat. Commun.* **2012**, *3*, 966.
22. Wei, H.; Ma, N.; Shi, F.; Wang, Z.; Zhang, X. Artificial Nacre by Alternating Preparation of Layer-by-Layer Polymer Films and $CaCO_3$ Strata. *Chem. Mater.* **2007**, *19*, 1974–1978.
23. Walther, A.; Bjurhager, I.; Malho, J.-M.; Pere, J.; Ruokolainen, J.; Berglund, L. A.; Ikkala, O. Large-Area, Lightweight and Thick Biomimetic Composites with Superior Material Properties via Fast, Economic, and Green Pathways. *Nano Lett.* **2010**, *10*, 2742–2748.
24. Shikinaka, K.; Aizawa, K.; Fujii, N.; Osada, Y.; Tokita, M.; Watanabe, J.; Shigehara, K. Flexible, Transparent Nanocomposite Film with a Large Clay Component and Ordered Structure Obtained by a Simple Solution-Casting Method. *Langmuir* **2010**, *26*, 12493–12495.
25. Chen, L.; Ballarini, R.; Kahn, H.; Heuer, A. H. Bioinspired Micro-Composite Structure. *J. Mater. Res.* **2007**, *22*, 124–131.
26. Bonderer, L. J.; Studart, A. R.; Gauckler, L. J. Bioinspired Design and Assembly of Platelet Reinforced Polymer Films. *Science* **2008**, *319*, 1069–1073.
27. Deville, S.; Saiz, E.; Nalla, R. K.; Tomsia, A. P. Freezing as a Path to Build Complex Composites. *Science* **2006**, *311*, 515–518.
28. Munch, E.; Launey, M. E.; Alsem, D. H.; Saiz, E.; Tomsia, A. P.; Ritchie, R. O. Tough, Bio-Inspired Hybrid Materials. *Science* **2008**, *322*, 1516–1520.
29. Erb, R. M.; Libanori, R.; Rothfuchs, N.; Studart, A. R. Composites Reinforced in Three Dimensions by Using Low Magnetic Fields. *Science* **2012**, *335*, 199–204.
30. Nakato, T.; Miyamoto, N. Liquid Crystalline Behavior and Related Properties of Colloidal Systems of Inorganic Oxide Nanosheets. *Materials* **2009**, *2*, 1734–1761.
31. Gabriel, J. C. P.; Davidson, P. New Trends in Colloidal Liquid Crystals Based on Mineral Moieties. *Adv. Mater.* **2000**, *12*, 9–20.
32. Tritschler, U.; Zlotnikov, I.; Zaslansky, P.; Aichmayer, B.; Fratzl, P.; Schlaad, H.; Cölfen, H. Hierarchical Structuring of Liquid Crystal Polymer–Laponite Hybrid Materials. *Langmuir* **2013**, *29*, 11093–11101.
33. El'nikova, L. V. Elastic Properties of Vanadium Pentoxide Aggregates and Topological Defects. *J. Supercond. Nov. Magn.* **2008**, *21*, 473–478.
34. Kaznacheev, A. V.; Bogdanov, M. M.; Taraskin, S. A. The Nature of Prolate Shape of Tactoids in Lyotropic Inorganic Liquid Crystals. *J. Exp. Theor. Phys.* **2002**, *95*, 57.
35. Zocher, H. Taktosole und Mesophasen. *Kolloid Z. Z. Polym.* **1954**, *139*, 81.
36. Zocher, H. Uber Freiwillige Strukturbildung in Solen. *Z. Anorg. Allg. Chem.* **1925**, *147*, 91–110.
37. Sonin, A. S. Inorganic Lyotropic Liquid Crystals. *J. Mater. Chem.* **1998**, *8*, 2557–2574.
38. Davidson, P. Vanadium Pentoxide Gels: From "Chimie Douce" to "Matière Molle". *C. R. Chim.* **2010**, *13*, 142–153.
39. Livage, J. Vanadium Pentoxide Gels. *Chem. Mater.* **1991**, *3*, 578–593.
40. Davidson, P.; Bourgaux, C.; Schoutteten, L.; Sergot, P.; Williams, C.; Livage, J. A Structural Study of the Lyotropic Nematic Phase of Vanadium Pentoxide Gels. *J. Phys. II* **1995**, *5*, 1577–1596.
41. Petkov, V.; Trikalitis, P. N.; Bozin, E. S.; Billinge, S. J. L.; Vogt, T.; Kanatzidis, M. G. Structure of $V_2O_5 \cdot nH_2O$ Xerogel Solved by the Atomic Pair Distribution Function Technique. *J. Am. Chem. Soc.* **2002**, *124*, 10157–10162.
42. Burghard, Z.; Leineweber, A.; van Aken, P. A.; Dufaux, T.; Burghard, M.; Bill, J. Hydrogen-Bond Reinforced Vanadia Nanofiber Paper of High Stiffness. *Adv. Mater.* **2013**, *25*, 2468–2473.
43. Davidson, P.; Batail, P.; Gabriel, J. C. P.; Livage, J.; Sanchez, C.; Bourgaux, C. Mineral Liquid Crystalline Polymers. *Prog. Polym. Sci.* **1997**, *22*, 913–936.
44. Livage, J. Synthesis of Polyoxovanadates via "Chimie Douce". *Coord. Chem. Rev.* **1998**, *178–180* (Part 2), 999–1018.
45. Lausser, C.; Cölfen, H.; Antonietti, M. Mesocrystals of Vanadium Pentoxide: A Comparative Evaluation of Three Different Pathways of Mesocrystal Synthesis from Tactosol Precursors. *ACS Nano* **2011**, *5*, 107–114.
46. Cölfen, H.; Antonietti, M. *Mesocrystals and Nonclassical Crystallization*; John Wiley & Sons, Ltd: New York, 2008.
47. Cölfen, H.; Antonietti, M. Mesocrystals: Inorganic Superstructures Made by Highly Parallel Crystallization and Controlled Alignment. *Angew. Chem., Int. Ed.* **2005**, *44*, 5576–5591.
48. Seto, J.; Ma, Y.; Davis, S. A.; Meldrum, F.; Gourrier, A.; Kim, Y.-Y.; Schilde, U.; Sztucki, M.; Burghammer, M.; Maltsev, S.; *et al*. Structure-Property Relationships of a Biological Mesocrystal in the Adult Sea Urchin Spine. *Proc. Natl. Acad. Sci. U.S.A.* **2012**, *109*, 3699–3704.
49. Floquet, N.; Vielzeuf, D. Ordered Misorientations and Preferential Directions of Growth in Mesocrystalline Red Coral Sclerites. *Cryst. Growth Des.* **2012**, *12*, 4805–4820.
50. Floquet, N.; Vielzeuf, D. Mesoscale Twinning and Crystallographic Registers in Biominerals. *Am. Mineral.* **2011**, *96*, 1228–1237.
51. Vielzeuf, D.; Floquet, N.; Chatain, D.; Bonneté, F.; Ferry, D.; Garrabou, J.; Stolper, E. M. Multilevel Modular Mesocrystalline Organization in Red Coral. *Am. Mineral.* **2010**, *95*, 242–248.
52. Vielzeuf, D.; Garrabou, J.; Baronnet, A.; Grauby, O.; Marschal, C. Nano to Macroscale Biomineral Architecture of Red Coral (Corallium Rubrum). *Am. Mineral.* **2008**, *93*, 1799–1815.
53. Rousseau, M.; Lopez, E.; Stempflé, P.; Brendlé, M.; Franke, L.; Guette, A.; Naslain, R.; Bourrat, X. Multiscale Structure of Sheet Nacre. *Biomaterials* **2005**, *26*, 6254–6262.
54. Li, X.; Chang, W.-C.; Chao, Y. J.; Wang, R.; Chang, M. Nanoscale Structural and Mechanical Characterization of a Natural Nanocomposite Material: The Shell of Red Abalone. *Nano Lett.* **2004**, *4*, 613–617.
55. Dauphin, Y. Nanostructures de la Nacre des Tests de Céphalopodes Actuels. *Paläontol. Z.* **2001**, *75*, 113–122.
56. Song, R.-Q.; Cölfen, H. Mesocrystals—Ordered Nanoparticle Superstructures. *Adv. Mater.* **2010**, *22*, 1301–1330.
57. Calderone, V. R.; Testino, A.; Buscaglia, M. T.; Bassoli, M.; Bottino, C.; Viviani, M.; Buscaglia, V.; Nanni, P. Size and Shape Control of $SrTiO_3$ Particles Grown by Epitaxial Self-Assembly. *Chem. Mater.* **2006**, *18*, 1627–1633.
58. Peng, Y.; Xu, A.-W.; Deng, B.; Antonietti, M.; Cölfen, H. Polymer-Controlled Crystallization of Zinc Oxide Hexagonal Nanorings and Disks. *J. Phys. Chem. B* **2006**, *110*, 2988–2993.
59. Qi, L.; Cölfen, H.; Antonietti, M.; Li, M.; Hopwood, J. D.; Ashley, A. J.; Mann, S. Formation of $BaSO_4$ Fibres with Morphological Complexity in Aqueous Polymer Solutions. *Chem.—Eur. J.* **2001**, *7*, 3526–3532.
60. Scherer, M. R. J.; Li, L.; Cunha, P. M. S.; Scherman, O. A.; Steiner, U. Enhanced Electrochromism in Gyroid-Structured Vanadium Pentoxide. *Adv. Mater.* **2012**, *24*, 1217–1221.
61. Wei, D.; Scherer, M. R. J.; Bower, C.; Andrew, P.; Ryhänen, T.; Steiner, U. A Nanostructured Electrochromic Supercapacitor. *Nano Lett.* **2012**, *12*, 1857–1862.
62. Cheng, K.-C.; Chen, F.-R.; Kai, J.-J. V_2O_5 Nanowires as a Functional Material for Electrochromic Device. *Sol. Energy Mater. Sol. Cells* **2006**, *90*, 1156–1165.
63. Lamarque-Forget, S.; Pelletier, O.; Dozov, I.; Davidson, P.; Martinot-Lagarde, P.; Livage, J. Electrooptic Effects in the Nematic and Isotropic Phases of Aqueous V_2O_5 Suspensions. *Adv. Mater.* **2000**, *12*, 1267–1270.

64. Huguenin, F.; Torresi, R. M. Investigation of the Electrical and Electrochemical Properties of Nanocomposites from V_2O_5, Polypyrrole, and Polyaniline. *J. Phys. Chem. C* **2008**, *112*, 2202–2209.
65. Hu, Y.-S.; Liu, X.; Müller, J.-O.; Schlögl, R.; Maier, J.; Su, D. S. Synthesis and Electrode Performance of Nanostructured V_2O_5 by Using a Carbon Tube-in-Tube as a Nanoreactor and an Efficient Mixed-Conducting Network. *Angew. Chem., Int. Ed.* **2009**, *48*, 210–214.
66. Muster, J.; Kim, G. T.; Krstić, V.; Park, J. G.; Park, Y. W.; Roth, S.; Burghard, M. Electrical Transport Through Individual Vanadium Pentoxide Nanowires. *Adv. Mater.* **2000**, *12*, 420–424.
67. Mai, L.; Xu, X.; Xu, L.; Han, C.; Luo, Y. Vanadium Oxide Nanowires for Li-Ion Batteries. *J. Mater. Res.* **2011**, *26*, 2175–2185.
68. Singhal, A.; Skandan, G.; Amatucci, G.; Badway, F.; Ye, N.; Manthiram, A.; Ye, H.; Xu, J. J. Nanostructured Electrodes for Next Generation Rechargeable Electrochemical Devices. *J. Power Sources* **2004**, *129*, 38–44.
69. Koltypin, M.; Pol, V.; Gedanken, A.; Aurbach, D. The Study of Carbon-Coated V_2O_5 Nanoparticles as a Potential Cathodic Material for Li Rechargeable Batteries. *J. Electrochem. Soc.* **2007**, *154*, A605–A613.
70. Patey, T. J.; Ng, S. H.; Büchel, R.; Tran, N.; Krumeich, F.; Wang, J.; Liu, H. K.; Novák, P. Electrochemistry of LiV_3O_8 Nanoparticles Made by Flame Spray Pyrolysis. *Electrochem. Solid-State Lett.* **2008**, *11*, A46–A50.
71. Schimmoeller, B.; Schulz, H.; Pratsinis, S. E.; Bareiss, A.; Reitzmann, A.; Kraushaar-Czarnetzki, B. Ceramic Foams Directly-Coated with Flame-Made V_2O_5/TiO_2 for Synthesis of Phthalic Anhydride. *J. Catal.* **2006**, *243*, 82–92.
72. Legrouri, A.; Baird, T.; Fryer, J. R. Electron Optical Studies of Fresh and Reduced Vanadium Pentoxide-Supported Rhodium Catalysts. *J. Catal.* **1993**, *140*, 173–183.
73. Nikolov, V.; Klissurski, D.; Anastasov, A. Phthalic Anhydride from o-Xylene Catalysis: Science and Engineering. *Catal. Rev. - Sci. Eng.* **1991**, *33*, 319–374.
74. Ramirez, R.; Casal, B.; Utrera, L.; Ruizhitzky, E. Oxygen Reactivity in Vanadium Pentoxide - Electronic-Structure amd Infrared-Spectroscopy Studies. *J. Phys. Chem.* **1990**, *94*, 8960–8965.
75. Wainwright, M. S.; Foster, N. R. Catalysts, Kinetics, and Reactor Design in Phthalic-Anhydride Synthesis. *Catal. Rev. - Sci. Eng.* **1979**, *19*, 211–292.
76. Colpaert, M. N. Exploratory Study of Catalytic Oxidation Reactions on Vanadium Pentoxide Single Crystals. *Z. Phys. Chem.* **1973**, *84*, 150–156.
77. Liu, J.; Wang, X.; Peng, Q.; Li, Y. Vanadium Pentoxide Nanobelts: Highly Selective and Stable Ethanol Sensor Materials. *Adv. Mater.* **2005**, *17*, 764–767.
78. Raible, I.; Burghard, M.; Schlecht, U.; Yasuda, A.; Vossmeyer, T. V_2O_5 Nanofibres: Novel Gas Sensors with Extremely High Sensitivity and Selectivity to Amines. *Sens. Actuators, B* **2005**, *106*, 730–735.
79. Mao, C.-J.; Pan, H.-C.; Wu, X.-C.; Zhu, J.-J.; Chen, H.-Y. Sonochemical Route for Self-Assembled V_2O_5 Bundles with Spindle-like Morphology and Their Novel Application in Serum Albumin Sensing. *J. Phys. Chem. B* **2006**, *110*, 14709–14713.
80. Biette, L.; Carn, F.; Maugey, M.; Achard, M. F.; Maquet, J.; Steunou, N.; Livage, J.; Serier, H.; Backov, R. Macroscopic Fibers of Oriented Vanadium Oxide Ribbons and Their Application as Highly Sensitive Alcohol Microsensors. *Adv. Mater.* **2005**, *17*, 2970–2974.
81. Amano, F.; Ito, T.; Takenaka, S.; Tanaka, T. Selective Photocatalytic Oxidation of Light Alkanes over Alkali-Ion-Modified V_2O_5/SiO_2; Kinetic Study and Reaction Mechanism. *J. Phys. Chem. B* **2005**, *109*, 10973–10977.
82. Amano, F.; Tanaka, T.; Funabiki, T. Steady-State Photocatalytic Epoxidation of Propene by O_2 over V_2O_5/SiO_2 Photocatalysts. *Langmuir* **2004**, *20*, 4236–4240.
83. Li, B.; Xu, Y.; Rong, G.; Jing, M.; Xie, Y. Vanadium Pentoxide Nanobelts and Nanorolls: From Controllable Synthesis to Investigation of Their Electrochemical Properties and Photocatalytic Activities. *Nanotechnology* **2006**, *17*, 2560.
84. André, R.; Natálio, F.; Humanes, M.; Leppin, J.; Heinze, K.; Wever, R.; Schröder, H. C.; Müller, W. E. G.; Tremel, W. V_2O_5 Nanowires with an Intrinsic Peroxidase-Like Activity. *Adv. Funct. Mater.* **2011**, *21*, 501–509.
85. Natalio, F.; Andre, R.; Hartog, A. F.; Stoll, B.; Jochum, K. P.; Wever, R.; Tremel, W. Vanadium Pentoxide Nanoparticles Mimic Vanadium Haloperoxidases and Thwart Biofilm Formation. *Nat. Nanotechnol.* **2012**, *7*, 530–535.
86. Donsanti, F.; Kostourou, K.; Decker, F.; Ibris, N.; Salvi, A. M.; Liberatore, M.; Thissen, A.; Jaegerman, W.; Lincot, D. Alkali Ion Intercalation in V_2O_5: Preparation and Laboratory Characterization of Thin Films Produced by ALD. *Surf. Interface Anal.* **2006**, *38*, 815–818.
87. Chan, C. K.; Peng, H.; Twesten, R. D.; Jarausch, K.; Zhang, X. F.; Cui, Y. Fast, Completely Reversible Li Insertion in Vanadium Pentoxide Nanoribbons. *Nano Lett.* **2007**, *7*, 490–495.
88. Patzke, G. R.; Krumeich, F.; Nesper, R. Oxidic Nanotubes and Nanorods—Anisotropic Modules for a Future Nanotechnology. *Angew. Chem., Int. Ed.* **2002**, *41*, 2446–2461.
89. Braithwaite, J. S.; Catlow, C. R. A.; Gale, J. D.; Harding, J. H. Lithium Intercalation into Vanadium Pentoxide: A Theoretical Study. *Chem. Mater.* **1999**, *11*, 1990–1998.
90. Spahr, M. E.; Stoschitzki-Bitterli, P.; Nesper, R.; Haas, O.; Novák, P. Vanadium Oxide Nanotubes. A New Nanostructured Redox-Active Material for the Electrochemical Insertion of Lithium. *J. Electrochem. Soc.* **1999**, *146*, 2780–2783.
91. Le, D. B.; Passerini, S.; Coustier, F.; Guo, J.; Soderstrom, T.; Owens, B. B.; Smyrl, W. H. Intercalation of Polyvalent Cations into V_2O_5 Aerogels. *Chem. Mater.* **1998**, *10*, 682–684.
92. Spahr, M. E.; Bitterli, P.; Nesper, R.; Müller, M.; Krumeich, F.; Nissen, H. U. Redox-Active Nanotubes of Vanadium Oxide. *Angew. Chem., Int. Ed.* **1998**, *37*, 1263–1265.
93. Dobley, A.; Ngala, K.; Yang, S.; Zavalij, P. Y.; Whittingham, M. S. Manganese Vanadium Oxide Nanotubes: Synthesis, Characterization, and Electrochemistry. *Chem. Mater.* **2001**, *13*, 4382–4386.
94. Krumeich, F.; Muhr, H. J.; Niederberger, M.; Bieri, F.; Schnyder, B.; Nesper, R. Morphology and Topochemical Reactions of Novel Vanadium Oxide Nanotubes. *J. Am. Chem. Soc.* **1999**, *121*, 8324–8331.
95. Galina, S. Z.; Viktor, L. V. Intercalation Compounds Based on Vanadium(V) Oxide Xerogel. *Russ. Chem. Rev.* **2003**, *72*, 311.
96. Park, N.-G.; Ryu, K. S.; Park, Y. J.; Kang, M. G.; Kim, D.-K.; Kang, S.-G.; Kim, K. M.; Chang, S.-H. Synthesis and Electrochemical Properties of V_2O_5 Intercalated with Binary Polymers. *J. Power Sources* **2002**, *103*, 273–279.
97. Livage, J. Actuator Materials: Towards Smart Artificial Muscle. *Nat. Mater.* **2003**, *2*, 297–299.
98. Wang, Y.; Takahashi, K.; Lee, K. H.; Cao, G. Z. Nanostructured Vanadium Oxide Electrodes for Enhanced Lithium-Ion Intercalation. *Adv. Funct. Mater.* **2006**, *16*, 1133–1144.
99. Gu, G.; Schmid, M.; Chiu, P.-W.; Minett, A.; Fraysse, J.; Kim, G.-T.; Roth, S.; Kozlov, M.; Munoz, E.; Baughman, R. H. V_2O_5 Nanofibre Sheet Actuators. *Nat. Mater.* **2003**, *2*, 316–319.
100. Börner, H. G.; Schlaad, H. Bioinspired Functional Block Copolymers. *Soft Matter* **2007**, *3*, 394–408.
101. Lee, M.; Cho, B.-K.; Zin, W.-C. Supramolecular Structures from Rod−Coil Block Copolymers. *Chem. Rev.* **2001**, *101*, 3869–3892.
102. Warren, S. C.; Messina, L. C.; Slaughter, L. S.; Kamperman, M.; Zhou, Q.; Gruner, S. M.; DiSalvo, F. J.; Wiesner, U. Ordered Mesoporous Materials from Metal Nanoparticle−Block Copolymer Self-Assembly. *Science* **2008**, *320*, 1748–1752.
103. Rey, A. D.; Herrera-Valencia, E. E. Liquid Crystal Models of Biological Materials and Silk Spinning. *Biopolymers* **2012**, *97*, 374–396.
104. Matranga, A.; Baig, S.; Boland, J.; Newton, C.; Taphouse, T.; Wells, G.; Kitson, S. Biomimetic Reflectors Fabricated Using Self-Organising, Self-Aligning Liquid Crystal Polymers. *Adv. Mater.* **2013**, *25*, 520–523.

105. Armatas, G. S.; Kanatzidis, M. G. Hexagonal Mesoporous Germanium. *Science* **2006**, *313*, 817–820.
106. Inagaki, S.; Guan, S.; Ohsuna, T.; Terasaki, O. An Ordered Mesoporous Organosilica Hybrid Material with a Crystal-Like Wall Structure. *Nature* **2002**, *416*, 304–307.
107. Yang, P.; Zhao, D.; Margolese, D. I.; Chmelka, B. F.; Stucky, G. D. Generalized Syntheses of Large-Pore Mesoporous Metal Oxides with Semicrystalline Frameworks. *Nature* **1998**, *396*, 152–155.
108. Yang, H.; Coombs, N.; Sokolov, I.; Ozin, G. A. Free-Standing and Oriented Mesoporous Silica Films Grown at the Air-Water Interface. *Nature* **1996**, *381*, 589–592.
109. Attard, G. S.; Glyde, J. C.; Goltner, C. G. Liquid-Crystalline Phases as Templates for the Synthesis of Mesoporous Silica. *Nature* **1995**, *378*, 366–368.
110. Qiu, H.; Inoue, Y.; Che, S. Supramolecular Chiral Transcription and Recognition by Mesoporous Silica Prepared by Chiral Imprinting of a Helical Micelle. *Angew. Chem., Int. Ed.* **2009**, *48*, 3069–3072.
111. Che, S.; Liu, Z.; Ohsuna, T.; Sakamoto, K.; Terasaki, O.; Tatsumi, T. Synthesis and Characterization of Chiral Mesoporous Silica. *Nature* **2004**, *429*, 281–284.
112. Shopsowitz, K. E.; Qi, H.; Hamad, W. Y.; MacLachlan, M. J. Free-Standing Mesoporous Silica Films with Tunable Chiral Nematic Structures. *Nature* **2010**, *468*, 422–425.
113. Gröschel, A. H.; Schacher, F. H.; Schmalz, H.; Borisov, O. V.; Zhulina, E. B.; Walther, A.; Müller, A. H. E. Precise Hierarchical Self-Assembly of Multicompartment Micelles. *Nat. Commun.* **2012**, *3*, 710.
114. Dupont, J.; Liu, G. ABC Triblock Copolymer Hamburger-Like Micelles, Segmented Cylinders, and Janus Particles. *Soft Matter* **2010**, *6*, 3654–3661.
115. Li, Z.; Hillmyer, M. A.; Lodge, T. P. Morphologies of Multicompartment Micelles Formed by ABC Miktoarm Star Terpolymers. *Langmuir* **2006**, *22*, 9409–9417.
116. Schleuss, T. W.; Abbel, R.; Gross, M.; Schollmeyer, D.; Frey, H.; Maskos, M.; Berger, R.; Kilbinger, A. F. M. Hockey-Puck Micelles from Oligo(p-benzamide)-b-PEG Rod−Coil Block Copolymers. *Angew. Chem., Int. Ed.* **2006**, *45*, 2969–2975.
117. Lagaly, G.; Schulz, O.; Zimehl, R. *Dispersionen Und Emulsionen*; Steinkopff: Darmstadt, Germany, 1997.
118. González, G.; Saraiva, S. M.; Aliaga, W. Isoelectric Points for Niobium and Vanadium Pentoxides. *J. Dispersion Sci. Technol.* **1994**, *15*, 249–249.
119. Hoffler, C. E.; Guo, X. E.; Zysset, P. K.; Goldstein, S. A. An Application of Nanoindentation Technique to Measure Bone Tissue Lamellae Properties. *J. Biomech. Eng.* **2005**, *127*, 1046–1053.
120. Kinney, J. H.; Balooch, M.; Marshall, S. J.; Marshall, G. W., Jr; Weihs, T. P. Hardness and Young's Modulus of Human Peritubular and Intertubular Dentine. *Arch. Oral Biol.* **1996**, *41*, 9–13.
121. Van Meerbeek, B.; Willems, G.; Celis, J. P.; Roos, J. R.; Braem, M.; Lambrechts, P.; Vanherle, G. Assessment by Nano-indentation of the Hardness and Elasticity of the Resin-Dentin Bonding Area. *J. Dent. Res.* **1993**, *72*, 1434–1442.
122. Gress, A.; Völkel, A.; Schlaad, H. Thio-Click Modification of Poly[2-(3-butenyl)-2-oxazoline]. *Macromolecules* **2007**, *40*, 7928–7933.
123. Zabler, S.; Cloetens, P.; Zaslansky, P. Fresnel-Propagated Submicrometer X-Ray Imaging of Water-Immersed Tooth Dentin. *Opt. Lett.* **2007**, *32*, 2987–2989.
124. Rack, A.; Zabler, S.; Müller, B. R.; Riesemeier, H.; Weidemann, G.; Lange, A.; Goebbels, J.; Hentschel, M.; Görner, W. High Resolution Synchrotron-Based Radiography and Tomography Using Hard X-Rays at the BAM-line (BESSY II). *Nucl. Instrum. Methods Phys. Res., Sect. A* **2008**, *586*, 327–344.
125. Schneider, C. A.; Rasband, W. S.; Eliceiri, K. W. NIH Image to ImageJ: 25 years of image analysis. *Nat. Methods* **2012**, *9*, 671–675.
126. Oliver, W. C.; Pharr, G. M. An Improved Technique for Determining Hardness and Elastic Modulus Using Load and Displacement Sensing Indentation Experiments. *J. Mater. Res.* **1992**, *7*, 1564–1583.
127. Wiesbrock, F.; Hoogenboom, R.; Leenen, M. A. M.; Meier, M. A. R.; Schubert, U. S. Investigation of the Living Cationic Ring-Opening Polymerization of 2-Methyl-, 2-Ethyl-, 2-Nonyl-, and 2-Phenyl-2-oxazoline in a Single-Mode Microwave Reactor. *Macromolecules* **2005**, *38*, 5025–5034.